الجمهورية الجزائرية الديمقراطية الشعبية
وزارة التعليم العالي والبحث العلمي

BADJ-MOKHTAR-ANNABA UNIVERSTY
UNIVERSITE-BADJ-MOKHTAR-ANNABA

جامعة باجي مختار-عنابة

Année 2026

Faculté des Sciences

Département de Physique

THESE

Présenté en vue de l'obtention de diplôme de

DOCTORAT

Par :

Hadjer Benmebarek

Quantum study of the pressure broadening phenomenon of the spectral profiles of alkali-rare-gas dimers

Option : Matière et Rayonnement

DIRECTEUR DE THESE : Nora Lamoudi Dr. Université d'Annaba.

Devant le jury

PRESIDENT :	**Hocine Meradji**	Prof. Université d'Annaba.
EXAMINATEURS :	**Kamel Alioua**	Prof. Université de souk-ahrass.
	Houria Triki	Prof. Université d'Annaba.

QUANTUM STUDY OF THE PRESSURE BROADENING PHENOMENON OF THE SPECTRAL PROFILES OF ALKALI-RARE-GAS DIMERS

A THESIS IN
PHYSICS

DOCTORAT

by
HADJER BENMEBAREK

2026

دراسة كمّية لظاهرة الاتساع الضغطي في المنحنيات الطيفية لثنائيات القلوية – الغازات النادرة

ملخص

تستخدم هذه الأطروحة نهجًا ميكانيكيًا كميًا لتحديد تأثيرات توسيع الضغط الملحوظة في الأجنحة البعيدة لخطي الرنين D_1 و D_2 للروبيديوم، المضطربة بوجود ذرات الأرجون. حُصل على منحنيات الطاقة الكامنة للحالات المنخفضة لجزيء $RbAr$ باستخدام مجموعتين مختلفتين من نقاط بيانات الجهد $ab-initio$. علاوة على ذلك ، حُسبت معاملات الامتصاص والانزياحات عند أطوال موجية تتراوح بين 500 و 900 نانومتر، وفي درجات حرارة تتراوح بين 500 و 3000 كلفن لكل مجموعة بيانات. تجدر الإشارة إلى أن طيف الامتصاص والانبعاث بين الانتقالات من النوع $\mathrm{B}^2\Sigma^+_{1/2} \rightarrow \mathrm{X}^2\Sigma^+_{1/2}$ يُظهر مزيجًا من الانتقالات التي تنتمي إلى فئتي الانتقال حر ـ حر و حر ـ مرتبط، مع كون الأخير هو النوع السائد. وقد ثبت وجود سمات القمر الأزرق عند طولي موجي 740 نانومترًا و 750 نانومترًا تقريبًا لمجموعتي البيانات الأولى والثانية على التوالي. وخضعت النتائج لتحليل مقارن بالبيانات التجريبية والدراسات النظرية السابقة.

Étude quantique du phénoméne d'élargissement de pression des profils spectraux des diméres alcalin-gaz rare.

Résumé

Cette thèse utilise une approche quantique pour déterminer les effets d'élargissement de pression observés dans les ailes lointaines des lignes de résonance D_1 et D_2 du rubidium perturbées par la présence des atomes d'argon. Les courbes d'énergie potentielle pour les états de basse énergie de la molécule RbAr ont été obtenues en utilisant deux série différentes des points des courbes ab-initio. De plus, les coefficients d'absorption et d'émission ont été calculés pour des longueurs d'onde comprises entre 500 et 900 nanométres et à des températures allant de 500 à 3000 Kelvin pour chaque série des données. Le spectre d'absorption et d'émission entre les transitions de type $B^2\Sigma^+_{1/2} \rightarrow X^2\Sigma^+_{1/2}$ mérite d'être mentionné, exhibant une combinaison de transitions de type libre-lié et libre-libre, cette derniére étant le type prédominant. Il a été démontré que des pics satellitaires bleus étaient présents á environ 740 nm et 750 nm pour la première et deuxième série des données ab-initio, respectivement. Les résultats ont été soumis á une analyse comparative avec des données expérimentales et des études théoriques antérieures.

Quantum study of the pressure broadening phenomenon of the spectral profiles of alkali-rare-gas dimers

ABSTRACT

This thesis employs a quantum mechanical approach to ascertain the pressure broadening effects observed in the far wings of the resonance lines D_1 and D_2 of rubidium, perturbed by the presence of the Argon atoms. The potential energy curves for the low-lying states of the RbAr molecule were obtained using two different sets of ab-initio potential data points. Furthermore, the absorption and emission coefficients were calculated at wavelengths between 500 and 900 nanometers and at temperatures ranging from 500 to 3000 Kelvin for each data set. The absorption and emission spectra between transitions of the type $B^2\Sigma^+_{1/2} \rightarrow X^2\Sigma^+_{1/2}$ is worthy of note, exhibiting a combination of the free-bound and free-free transitions, with the latter being the predominant type. It was demonstrated that the blue satellite features were present at approximately 740 nm and 750 nm for the first and second data sets, respectively. The findings were subjected to a comparative analysis with experimental data and previous theoretical studies.

الإهداء

الحمد لله الذي بلطفه تُضاء الطرق، وبعونه يشتدّ العزم، وبتوفيقه وصلتُ إلى هذا المقام.

إلى نفسي التي حملت صبرًا يفوق الكلمات، ومضت بثبات رغم ثِقل الطريق.

إلى ابني أحمد، فرح قلبي وجوده علمني القوة الحقيقية والصبر الجميل الدي يحعل المستحيل ممكن.

إلى أبي، سند الروح ووقارها، الذي تعلمت منه أن الخطى لا تُوزن إلا بالصدق.

إلى أمي، الحضن الذي لا يبلى، والدعاء الذي يرافقني أينما ذهبت.

إلى إخوتي، رفقاء النشأة الأولى، الذين يثبتون دائمًا أن العائلة وطنٌ لا يتغيّر.

إلى أصدقائي، الذين جاء حضورهم لطفًا في أوقات العتمة.

إلى أساتذتي، الذين غرسوا في داخلي احترام العلم ، وفتحوا لي أبواب المعرفة بكرمهم.

إلى طلابي وتلاميذي، من أهدوني معنى الرسالة، وأيقظوا في قلبي شغف التعليم .

إلى كل من مدّ لي يدًا في هذا العمل، ولو بكلمة طيّبة أو إشارة نور.

وحتى الذين لم يساعدوني، الدين ادوني، والدين غلقوا الابواب في وجهي لهم مكان في هذا الطريق، فلولاهم ما اكتملت حكمة التجربة.

أهدي هذا العمل إلى الجميع إلى كل قلب عبر في طريقي وترك أثرًا يليق بالامتنان.

ACKNOWLEDGEMENTS

I thank Allah Almighty for His blessings, guidance, and strength throughout this journey.

I extend my deepest gratitude to my parents for their unwavering support and encouragement.

I am profoundly grateful to Doctor Nora LAMOUDI, whose exceptional guidance and unwavering dedication went far beyond the role of a supervisor. Her commitment, support, and constant attention were instrumental in shaping the quality and completion of this work.

My appreciation is also extended to the defense committee members: Professor Hocine MERADJI, a faculty member at Annaba University, chaired the thesis jury; Professor Kamel ALIOUA, a faculty member at Cherif Messaadia University Souk Ahras; and Professor Houria TRIKI, a faculty member at Badji Mokhtar University of Annaba, for taking the time to examine my dissertation and for their helpful comments.

I would especially want to thank Professors Mohamed Tahar BOUAZZA, Rafik CHAMMAM, and Chawki BENSELEM for their unwavering support, which inspired me to keep going and never give up.

CONTENTS

ILLUSTRATIONS

TABLES

Introduction

The broadening of the alkali-rare gas diatomic systems associated with the D_1 and D_2 resonance transitions has long attracted considerable attention. In particular, the exploitation of the far-wing broadening of the alkali D_1 and D_2 lines caused by collisions with rare gas atoms has proven crucial in addressing several challenges related to the development of high-power laser systems [1–3]. In pumped alkali lasers, the laser operation relies on the optical excitation of satellite structures that emerge in the blue wings of the rubidium and cesium D_2 transitions [2,4,5]. Beyond laser applications, alkali metal resonance lines broadened through interactions with rare gas perturbers play an essential role in astrophysics. Accurate modeling of these broadened profiles enables the diagnosis of planetary atmospheres and the determination of the chemical and physical properties of brown dwarfs [6,7]. In this work, we focus on the investigation of the far-wing structures of rubidium spectra arising from the collisional broadening of the D_1 and D_2 lines by argon atoms. To this end, absorption and emission coefficients are computed using fully quantum mechanical formulations. Calculations are performed over a range of temperatures and for two different sets of interaction potentials in order to assess both temperature and potential-energy effects. Particular attention is devoted to the analysis of the blue and red wings of the spectra, as well as to the localization and physical origin of possible satellite features. Early experimental investigations of RbAr absorption and emission spectra were conducted in the 1970s by Drummond and Gallagher [8], followed by measurements reported by Dubourg et al. [9]. These studies were primarily aimed at extracting information on the ground- and excited-

state interaction potentials. More recently, renewed interest in the RbAr system has emerged. Loperand and Weeks [10] employed quantum mechanical calculations to determine the pressure broadening and line shifts of the D_1 and D_2 line cores of rubidium atoms in argon gas, while Li-Chung Ha et al. [11] experimentally measured the pressure-dependent broadening of the D_1 line.

Over the past decade, detailed measurements of the far-wing line shapes of the D_1 and D_2 resonance transitions of rubidium in argon buffer gas have been reported in both absorption and emission by Moroshkin et al. [12], Rice et al. [13], and Ockenfels et al. [14]. In addition, Moroshkin [12] theoretically evaluated the absorption and emission profiles using the unified theory of spectral line broadening. Despite these efforts, laboratory experiments consistently reveal the presence of a blue satellite associated with the D_2 transition, which is not reproduced by theoretical profiles obtained using classical approaches.

The results of these previous experimental and theoretical studies provide an important benchmark for comparison with the pressure-broadened profiles calculated in the present work. In order to understand these phenomena in a comprehensive way, this study is divided into three main chapters:

Chapter 1: Theoretical Investigation

Chapter one is devoted to the treatment of quantum theory, establishing the formula for reduced absorption coefficients. It begins with an analytical development based on Maxwell-Boltzmann statistics to obtain expressions for the number of

molecular states. The quantum dipole approximation and the classical treatment of electromagnetic radiation are used to establish the molecular transition probability, expressed by Fermi's golden rule. The problem of binary elastic collisions is then addressed using the adiabatic Born-Oppenheimer approximation, which separates the motion of the nuclei from that of the electrons. In the centre-of-mass system, the interaction of two atoms is reduced to the elastic diffusion of a fictitious particle through a diffusing centre characterised by the interatomic potential. This leads to a time-independent and one-dimensional Schrödinger equation, the numerical solution of which provides the free and bound state wave functions necessary to calculate the reduced absorption coefficients. Finally, the chapter gives the mathematical expressions for the reduced absorption and emission coefficients for the free-bound and free-free transitions.

Chapter 2: Potentials Energy Curves and Transition Dipole Moment Construction

The second chapter presents the method used to construct the potential energy curves (PECs) for the molecular symmetries correlated with the interaction of a rubidium atom in its ground state Rb(5s) or in its first excited state Rb(5p) with an argon atom in its ground state by using two distinct sets of potential data points . Some spectroscopic parameters, such as equilibrium radii and potential well depths are then compared with existing results to ensure accuracy and the reliability of the potential curves. In addition, this chapter details the construction

of transition dipole moments (TDMs), which link the ground state of the rubidium atom to various excited states.

Chapter 3: Results and Discussion

The third and final chapter presents the details of the calculations and the results obtained for the absorption coefficients. The photoabsorption spectra based on two sets of potential data, RbAr, are analyzed at different temperatures. We specify the positions and origins of the satellites appearing in the far wings of the spectra and detail the contributions of each allowed transition. We also study the effect of temperature on the spectral profiles, focusing in particular on the positions and intensities of the satellites. A comparative analysis is carried out for the spectra close to the satellite, at wavelengths around "750 nm" for set I and around "740 nm" for set II, with reference to previously obtained results. Furthermore, we present the results of the redistribution photoemission spectra of the RbAr system for the two sets potential at two different temperatures, T=500 K and T=1000 K. We compare the positions of the selected satellites with the experimental results documented and provide a comprehensive discussion of the agreement and discrepancies observed. The conclusion of the chapters provides a summary of the results, discussing their implications for the comprehension of atomic interactions. and we will conclude with a general conclusion.

Chapter 1:

Theoretical Investigation

CHAPTER 1

THEORETICAL INVESTIGATION

It is widely recognized in the field of atomic and molecular spectroscopy that when an atom, situated in a radiation field, collides with the atoms of its surrounding environment, alterations occur in the spectral profiles of the emitting atom. These modifications can be categorized into two distinct phenomena [15, 16]. The initial alteration transpires within the central region of the resonance line and is characterized by an augmentation, often accompanied by displacement, of these lines. The subsequent alteration influences the wings of the spectral profiles, wherein the appearance of minor peaks, known as satellites, is observed. These two phenomena, referred to as collisional enlargement, are respectively denoted as pressure expansion in the heart and pressure expansion in the wings [17, 18].

In this research, we are interested in studying the pressure broadening phenomenon resulting from the interaction of rubidium atoms by argon atoms in the far wings of the absorption spectrum. This occurs when a photon with energy h_ν is absorbed by an excited Rb(5s) atom, allowing it to interact with the perturbing Ar($3s^2\ 3p^6$) atoms and reach the excited state Rb(5p).

During the course of this particular procedure, the quasi-molecule that is produced undergoes a transition from its fundamental state, Rb(5s) + Ar($3s^2\ 3p^6$) to the initial excited state Rb($5p_{1/2}$) + Ar ($3s^2\ 3p^6$) and Rb($5p_{3/2}$) + Ar ($3s^2\ 3p^6$). In the field of spectroscopy, this occurrence is identified and described by the ab-

sorption coefficient.

1.1 Absorption Coefficient

The Beer-Lambert law may be used to estimate the empirically determined absorption coefficient, which is a physical quantity [19].

$$I(\nu) = I_0 \exp(-k_\nu l). \tag{1.1}$$

When $k_\nu = k(\nu)$ is the absorption coefficient, which depends on the frequency of the radiation employed, and $I(\nu)$ is the intensity of the radiation transmitted, I_0 is the intensity of the incoming radiation of frequency ν that passes through the absorbing medium of thickness l .

The direct measurement of I, I_0 and l allows us to determine the absorption coefficient k_ν. A more accurate calculation of the absorption coefficient can be achieved by using a purely quantum treatment that connects the macroscopic magnitude k_ν to the microscopic grandeur's of the absorbing medium.

The absorption coefficient can be characterized as the quantity of photons that are assimilated within a specific duration of time, a specific volume range, and a specific frequency range [20]. A radiating atom interacting with a perturbing atom undergoes a transition from a lower initial state $|i\rangle$to a higher final state $\langle f|$ during photoabsorption. This process's absorption coefficient,k_{if}, is provided by the relation [21]

$$k_{if} = \frac{p_{if} N_i}{F} \tag{1.2}$$

where

- p_{if} is the transition probability per molecular state per unit time.
- N_i is the molecular density.
- F is the flux of photons incident on the molecule per unit area and per unit time.

To obtain the expression for k_{if}, we need to explain separately the three terms on the right-hand side of the equation (1.2).

1.1.1 Transition Probability

Let's consider a system consisting of a pair of atoms in their initial state $|i\rangle$ of energy E" subjected to electromagnetic radiation produced by an electric field **E**. Under the influence of this radiation, the pair of atoms transitions to a final state $\langle f|$ of energy E'. In this case, the transition probability per unit time and per unit initial wave vector density is given by Fermi's golden rule [22, 23] .

$$p_{if} = \frac{2\pi}{\hbar}|\langle f|W|i\rangle|^2 \rho_f\left(E'\right) \tag{1.3}$$

where $\rho_f\left(E'\right)$ is the final state density and W is an additional energy introduced into the system by the electromagnetic wave acting on the electronic dipole moment p of the formed atomic dimer. This energy appears as an additional term in the Hamiltonian of the Schrôdinger equation governing the motion of the radiator-perturber dimer and acts as a time-dependent perturbation, expressed in the dipole approximation by [23].

$$W = -\mathbf{p} \cdot \mathbf{E} \tag{1.4}$$

where $\mathbf{p}$ is the dipole moment defined by $\mathbf{p} = -e\mathbf{r}$, with $\mathbf{r}$ being the set of vectors $\mathbf{r_i}$ of the electrons of charge $\mathbf{e}$. The electric field $\mathbf{E}$ varies harmonically according to the relation

$$\mathbf{E} = E_0 \cos(2\pi\nu t)\mathbf{e}, \tag{1.5}$$

$$\mathbf{E} = \frac{E_0}{2}\left(e^{+2i\pi\nu t} + e^{-2i\pi\nu t}\right)\mathbf{e}. \tag{1.6}$$

Here $\mathbf{e}$ represents the unit vector in the direction of polarization of the electromagnetic wave and $\mathbf{E_0}$ is the amplitude of the associated electric field. By replacing the dipole moment $\mathbf{p}$ and the electric field E with their explicit forms. The perturbation W becomes by substituting the explicit forms of the dipole moment ($\mathbf{p}$) and the electric field ($\mathbf{E}$).

$$W = \frac{eE_0}{2}\left(e^{+2i\pi\nu t} + e^{-2i\pi\nu t}\right)\mathbf{er} \tag{1.7}$$

In the case where the incident radiation is assumed to be isotropic and unpolarized, the orientation of the unit vector $\mathbf{e}$ is therefore random. The average $|\mathbf{er}|^2_{moy}$ is thus equal to $\frac{1}{3}|\mathbf{r}|^2$ and equation (1.3) becomes [24]

$$p_{if} = \frac{\pi^2 E_0}{3\hbar}|\langle f|e\mathbf{r}|i\rangle|^2 \rho_f\left(E'\right) \tag{1.8}$$

1.1.2 Incident Photon Flux

The flux of incident photons is the time average of the real part of the Poynting vector S divided by the energy of a photon $h\nu$ [25]

$$F = \frac{1}{h\nu}\langle \mathbf{S}\rangle_{\mathrm{moy}} \tag{1.9}$$

$$F = \frac{cU_{\text{moy}}}{h\nu} \tag{1.10}$$

where c is the speed of light in a vacuum and U is the energy density per unit volume transported by the electromagnetic wave given by the following formula [25]

$$U = \frac{1}{8\pi}\left(\mathbf{E}^2 + c^2\mathbf{B}^2\right). \tag{1.11}$$

The vectors **E** and **B** represent the electric and magnetic fields of the electromagnetic wave, respectively. For plane electromagnetic waves, these vectors are perpendicular to each other. The electric field **E** is defined by equation (1.5) and the magnetic field **B** is given by

$$\mathbf{B} = B_0 \cos(2\pi\nu t)\mathrm{e}_1 \tag{1.12}$$

with $\mathbf{e}_1$ being a unit vector perpendicular to **e**. The amplitudes B_0 and E_0 are related by the relation

$$B_0 = \frac{E_0}{c} \tag{1.13}$$

In this context, The equation (1.11) transforms into

$$U = \frac{1}{8\pi}\left(E_0^2 + c^2B_0^2\right)\cos^2(2\pi\nu t) \tag{1.14}$$

The average energy density U_{moy} per unit volume is defined as the time average of the energy density U

$$U_{\text{moy}} = \frac{1}{T}\int_0^T U dt \tag{1.15}$$

$$U_{\text{moy}} = \frac{1}{8\pi}E_0^2 \tag{1.16}$$

were $T = 1/\nu$ is the period. Substituting equation (1.16) into equation (1.10), the incident flux will thus be

$$F = \frac{cE_0^2}{8\pi h\nu}. \tag{1.17}$$

1.1.3 Molecular Density of State

The number of molecules formed per unit volume is known as the molecular density of state. We will denote the number of free atoms of type A and B by N_A and N_B and the number of molecules formed by N_{AB}. The partition functions of atoms A, B and the molecule AB at thermodynamic equilibrium are given by the equations $Z_A(T)$, $Z_B(T)$ and $Z_{AB}(T)$ respectively. The Maxwell-Boltzmann partition laws are often followed by these functions [26].

$$\frac{N_{AB}}{N_A N_B} = \frac{\mathcal{Z}_{AB}(T)}{\mathcal{Z}_A(T)\mathcal{Z}_B(T)} \tag{1.18}$$

were

$$Z_A(T) = z_A V \left(\frac{2\pi m_A k_1 T}{h^2}\right)^{3/2} \exp\left(-\frac{E_A}{k_\beta T}\right) \tag{1.19}$$

$$Z_B(T) = z_B V \left(\frac{2\pi m_B k_{11} T}{k^2}\right)^{3/2} \exp\left(-\frac{E_B}{k_\beta T}\right) \tag{1.20}$$

$$Z_{AB}(T) = z_{AB} V \left(\frac{2\pi m_{AB} k_B T}{h^2}\right)^{3/2} \exp\left(-\frac{E_{AB}}{k_\beta T}\right) \tag{1.21}$$

where V is the volume at which the system in question evolves and k_β is Boltzman's constant. The partition functions of the internal degrees of freedom of the atoms A and B and the molecule AB are represented by the physical numbers z_A, z_B and

z_{AB} and their corresponding energies are E_A, E_B and E_{AB}. Given that the reduced mass of the system is

$$\mu = \frac{m_A m_B}{m_A + m_B}, \tag{1.22}$$

and its total mass is

$$m_{AB} = m_A + m_B \tag{1.23}$$

By subtraction of equations (1.16), (1.17) and (1.18) from relation (1.15) we obtain

$$\frac{N_{AB}}{N_A N_B} = \frac{1}{V}\frac{z_{AB}}{z_A z_B}\left(\frac{h^2}{2\pi\mu k_B T}\right)^{3/2} \exp\left(-\frac{E_n}{k_B T}\right) \tag{1.24}$$

were E_n is the kinetic energy of the nuclei and k_i is the relative wave vector of the colliding pair in an initial state $|i\rangle$

$$E_n = E_{AB} - (E_A + E_B) = \frac{\hbar^2 K_i^2}{2\mu} \tag{1.25}$$

Ratio $\frac{z_{AB}}{z_A z_B}$ denoted by ω includes all internal electronic degrees of rotational freedom [27], It is also expressed in the following ways

$$\omega = \frac{2 - \delta_{0,\Lambda'+\Lambda"}}{2 - \delta_{0,\Lambda"}} \frac{(2S_{AB}+1)}{(2S_A+1)(2S_B+1)} \tag{1.26}$$

The multiplicities of the molecular spins of atom A, atom B, and dimer AB are denoted as S_{AB}, S_A and S_B , respectively. The initial ratio, which is $\left(2 - \delta_{0,\lambda'+\Lambda"}\right) / \left(2 - \delta_{0,\Lambda"}\right)$, signifies the degeneracy of electronic states. We put $n_A = N_A/V$ and $n_B = N_B/V$ is the molecular state density that is then defined by defining $N_i = N_{AB}/V$.

$$N_i = n_A n_B \omega \left(\frac{h^2}{2\pi\mu k_\beta T}\right)^{3/2} \exp\left(-\frac{\hbar^2 K_i^2}{2\mu k_\beta T}\right). \tag{1.27}$$

The absorption coefficient expression may be expressed as follows by replacing equations (1.8), (1.17), and (1.27) in (1.2).

$$\alpha_{if} = n_A n_B \left(\frac{h^2}{2\pi\mu k_B T}\right)^{3/2} \left(\frac{8\pi^3\nu}{3c}\right) \exp\left(-\frac{\hbar^2 K_i^2}{2\mu k_B T}\right) |\langle f| \,\mathrm{er}\, |i\rangle|^2 \rho_f\left(E'\right). \quad (1.28)$$

The evaluation of the matrix element denoted as $\langle f|er|i\rangle$is contingent upon the prior determination of the wave functions of the initial quantum states $|i\rangle$, as well as the final quantum states $|f\rangle$. In order to achieve this, it is imperative to solve the Schrödinger equation specifically for a system consisting of two atoms that are interacting with one another, a task that is fundamentally grounded in the theoretical framework of binary collision theory, which elucidates the interactions and dynamics between such particles. Consequently, this theoretical framework will be elaborated upon in the subsequent discourse.

1.2 Theory of Binary Collisions

In this part of section, we look at the theoretical framework that is essential for understanding the physics of collisions. Our focus will be on binary collisions involving two interacting particles. This limitation is particularly relevant when studying dilute gases, where three-body collisions are sufficiently rare to be neglected.

Binary collisions are the simplest form of collision and provide a fundamental understanding that can be extended to more complex interactions. We consider the elastic and non-relativistic collisions of two atoms, labelled A and B. In an elastic collision the total kinetic energy of the system is conserved, and non-relativistic

means that the velocities of the particles are much less than the speed of light, so relativistic effects can be ignored.

The theoretical treatment of these collisions involves quantum mechanics, and we use the time-independent Schrödinger equation to describe the motion of the atoms. The Schrödinger equation is given by

$$H\Psi = E_T\Psi \tag{1.29}$$

The Hamiltonian operator, denoted H, is used to represent the total energy of the system, while Ψ symbolises the total wave function associated with the system of two particles with a total energy denoted E_T. If m_A, m_B and m_e are used to symbolise the respective masses of the nuclei of atoms A and B and the electrons e, and R and r indicate their position vectors measured with respect to a fixed reference frame, the Hamiltonian H of the system can be represented by

$$H = -\sum_{l=A,B}\frac{\hbar^2}{2m_l}\nabla^2_{R_l} - \frac{\hbar^2}{2m_e}\sum_{i=1}^{N}\nabla^2_{r_i} + V_{el}\left(\mathbf{R}_{A,B}, r\right) + V_N\left(\mathbf{R}_{A,B}\right) \tag{1.30}$$

where $\hbar$ is the reduced Planck constant and N is the total number of electrons. The first term represents the kinetic energy of the two nuclei and the second that of the electrons. The next term is the potential energy of the electrons in the ion field. The last term is the potential energy between the two nuclei. Since the mass of the electrons is much smaller than that of the nuclei, the motion of the two interacting particles can be separated into two independent motions: that of the electrons and that of the nuclei. This significant simplification, known as the Born-Oppenheimer approximation [24], allows us to write the wave function$\varphi(R_{A,B,r})$ as a product of a

function of the electronic wave $\varphi_e l\left(\mathrm{R}_{A,B}, r\right)$ and a nuclear wave $\varphi_N\left(\mathrm{R}_{A,B}\right)$, i.e.

$$\Psi\left(\mathrm{R}_{A,B}, r\right) = \varphi_{el}\left(\mathrm{R}_{A,B}, r\right)\varphi_N\left(\mathrm{R}_{A,B}\right). \tag{1.31}$$

The wave function $\varphi_{el}\left(\mathrm{R}_{A,B} r\right)$ will be a solution of the Schrödinger equation relating to the motion of the electrons when the nuclei are fixed at positions R, which gives

$$\begin{aligned} H_{el}\varphi_{el}\left(\mathrm{R}_{A,B}, r\right) &= \left\{-\frac{\hbar^2}{2m_e}\sum_{i=1}^{N}\nabla^2_{r_d}\left(\mathrm{R}_{A,B}, r\right)\right\}\varphi_{el}\left(\mathrm{R}_{A,B}, r\right) \\ &= E_{el}\left(\mathrm{R}_{A,B}\right)\varphi_d\left(\mathrm{R}_{A,B}, r\right) \end{aligned} \tag{1.32}$$

Let us now apply the Hamiltonian H given by equation (1.30) to the wave function $\Psi\left(\mathbf{R}_{A,B}, r\right)$ defined in (1.31). We easily obtain the relation

$$H\Psi\left(\mathrm{R}_{A,B}, r\right) = \left\{-\sum_{l=A,B}\frac{\hbar^2}{2m_l}\nabla^2_{R_l} + H_{el} + V_N\left(\mathrm{R}_{A,B}\right)\right\}\varphi\left(\mathrm{R}_{A,B}, r\right) \tag{1.33}$$

Using the equation (1.31) and the general property

$$\nabla^2(f\cdot g) = f\nabla^2 g + 2\nabla f\cdot\nabla g + g\nabla^2 f \tag{1.34}$$

From the Laplacian we easily get the relation

$$\begin{aligned} H\Psi\left(\mathbf{R}_{A,B}, r\right) = \varphi_{el}\left(\mathbf{R}_{A,B}, r\right)&\left\{-\sum_{l=A,B}\frac{\hbar^2}{2m_l}\nabla^2_{R_d} + E_{el}\left(\mathbf{R}_{A,B}\right) + V_N\left(\mathbf{R}_{A,B}\right)\right\}\varphi_N\left(\mathbf{R}_{A,B}\right) \\ &- \sum_{l=A,B}\frac{\hbar^2}{2m_l}\left[2\nabla_{R_l}\varphi_N\cdot\nabla_{R_l}\varphi_{el} + \varphi_N\nabla^2_{R_l}\varphi_{el}\right]. \end{aligned} \tag{1.35}$$

The last term is related to the ratio m_ε/m_l, which is very small [28]. It can therefore be neglected. The dynamics of the nuclei of the system is finally obtained by solving the equation

$$\left\{-\sum_{l=A,B}\frac{\hbar^2}{2m_l}\nabla^2_{R_l}+V\left(\mathrm{R}_{A,B}\right)\right\}\varphi_N\left(\mathrm{R}_{A,B}\right)=E_T\varphi_N\left(\mathrm{R}_{A,B}\right), \tag{1.36}$$

whose effective field $V\left(\mathrm{R}_{A,B}\right)=E_{el}\left(\mathrm{R}_{A,B}\right)+V_N\left(\mathrm{R}_{A,B}\right)$ is known as the potential energy curve of the diatomic molecule [27]. For simplicity it is better to switch from the laboratory coordinates to the coordinates of the centre of mass of the two nuclei. To do this, we define the position vector of the centre of mass of the atomic system as follows

$$\rho=\frac{m_A\mathrm{R}_A+m_B\mathrm{R}_B}{m_A+m_B} \tag{1.37}$$

and we write the total mass of the system $M_{\mathrm{tot}}=m_{AB}=m_A+m_B$ and its reduced mass $\mu=m_Am_B/M_{\mathrm{tot}}$. By denoting the relative vector between the two nuclei by $\mathbf{R}=\mathbf{R}_A-\mathbf{R}_B$, the new form of equation (1.36) becomes

$$\left\{-\frac{\hbar^2}{2M_{td}}\nabla^2_\rho-\frac{\hbar^2}{2\mu}\nabla^2_{\mathbf{R}}+V(\mathbf{R})\right\}\varphi_N(\rho,\mathbf{R})=E_T\varphi_N(\rho,\mathbf{R}). \tag{1.38}$$

Given that the Born-Oppenheimer approximation renders the potential energy function $V(R)$ dependent solely on the relative position vector $\mathbf{R}$, it is possible to decompose the wave function $\varphi_N(\rho,\mathbf{R})$ in the following manner:

$$\varphi_N(\rho,\mathbf{R})=\varphi_N(\rho)\times\varphi_N(\mathbf{R}) \tag{1.39}$$

The functions $\varphi_N(\rho)$ and $\varphi_N(\mathrm{R})$ are subject to the following separate equations.

$$-\frac{\hbar^2}{2M_{td}}\nabla^2_\rho\varphi_N(\rho)=E_\rho\varphi_N(\rho) \tag{1.40}$$

$$\left\{-\frac{\hbar^2}{2\mu}\nabla^2_{\mathrm{R}}+V(\mathrm{R})\right\}\varphi_N(\mathbf{R})=E\varphi_N(\mathrm{R}) \tag{1.41}$$

In this context, $E = E_T - E_\rho$ were E_ρ represents the centre of mass energy, whose motion is described by the following equation (1.41): In the centre of mass reference frame, the centre of mass is at rest, and the collision will therefore be described by the wave equation (1.41) only. This equation demonstrates that the collision of two atoms can be reduced to a problem of diffusion of a single particle of reduced mass μ immersed in a potential field V(R). In order to solve the wave equation (1.41), it is necessary to assume that the movement of the nuclei takes place in a central potential. This implies that the potential does not depend on the direction of the position vector $\mathbf{R}$, but only on its modulus, $R = |R|$. Furthermore, the new form of the wave function $\varphi_N(R)$ can be expressed as a product of a purely radial function, denoted as $\Psi_N(R)$, which is associated with the relative movement of the nuclei, and a spherical harmonic, $\Upsilon_J^m(\theta, \varphi)$, which is linked to their rotation.

$$\varphi_N(\mathbf{R}) = \frac{\Psi_J(R)}{R} \Upsilon_J^m(\theta, \varphi) \tag{1.42}$$

The variables θ and Ψ correspond to the polar and azimuthal angles, in that order. The spherical harmonics $\Upsilon J_m(\theta, \varphi)$ are the common eigen functions of the operators J^2 and J_z, the projection of the orbital angular momentum J on the z axis, which satisfy the eigenvalue equations.

$$J^2 \Upsilon_J^\infty(\theta, \varphi) = J(J+1)h^2 \Upsilon_i^m(\theta, \varphi) \tag{1.43}$$

$$J_z \Upsilon_l^m(\theta, \varphi) = m\hbar \Upsilon_l^m(\theta, \varphi). \tag{1.44}$$

The quantum number J can take all possible integer values $J \geq 0$, while the magnetic quantum number m is bounded by the inequality $-J \leqslant m \leqslant +J$. For convenience

it is better to express the wave equation in spherical coordinates. The Laplacian ∇_R^2 appearing in equation (1.41)

$$\nabla_R^2 = \frac{1}{R^2}\frac{\partial}{\partial R}\left(R^2\frac{\partial}{\partial R}\right) - \frac{J^2}{\hbar^2 R} \tag{1.45}$$

By substituting equation (1.42) into (1.41) and using (1.43), (1.44) and (1.45), the radial wave functions become solutions of the radial wave equation

$$\frac{d^2\Psi_J(R)}{dR^2} + \frac{2\mu}{\hbar^2}\left\{E - V(R) + \frac{\hbar^2}{2\mu}\frac{J(J+1)}{R^2}\right\}\Psi_J(R) = 0. \tag{1.46}$$

The solution of this one-dimensional equation will yield the radial wave functions. When $E < 0$, the quantum states are described as bound, with the wave functions given by $\Psi_J(R) = \Psi_{\nu,J}(R)$, characterized by the vibrational quantum number v, the rotational quantum number J, these wave functions satisfy the orthonormalization relation.

$$\int_0^\infty \Psi^*_{v,J}(R)\Psi_{v',J'}(R)\,dR = \delta_{vv'}\delta_{JJ'} \tag{1.47}$$

The δ is the well-known Kronecker symbol. For the case where $E > 0$, the quantum states are said to be free and belong to a continuum of energy $E = \epsilon$. The wave functions are written in the form $\Psi_J(R) = \Psi_{\epsilon,J}(R)$. Since they are not square-integrable, these wave functions are normalized with respect to the energy [22] according to the relation

$$\int_0^\infty \Psi^*_{\epsilon,J}(R)\Psi_{\epsilon',J'}(R)\,dR = \frac{\pi}{2}\delta(\epsilon - \epsilon'). \tag{1.48}$$

$\delta(\epsilon - \epsilon')$ is the Dirac delta function [29].

1.3 Different Types of Electronic Transitions

In the study of electronic transitions within atoms and molecules, understanding the absorption of electromagnetic radiation is crucial. These transitions, characterized by changes in the electronic state from lower to higher energy levels, exhibit distinct absorption behaviors depending on the initial and final states of the electron involved.

In the preceding discussion, it becomes evident that the absorption coefficient for a transition from a lower electronic state to a higher one can be deconstructed into four distinct components. These components correspond to the four possible types of transitions:

- Bound-Bound (b-b): This refers to transitions between two bound electronic states.
- Bound-Free (b-f): This refers to transitions from a bound electronic state to a free electronic state.
- Free-Bound (f-b): This refers to transitions from a free electronic state to a bound electronic state.
- Free-Free (f-f): This refers to transitions between two free electronic states.

Through this structured exploration, we seek to unveil the intricate interplay between electronic transitions and absorption coefficients, thereby laying the foundation for deeper insights into optical and spectroscopic analyses in diverse scientific

disciplines.

1.3.1 Free-Bound Transitions

The absorption coefficient for a free-bound transition is obtained by integrating equation (1.28) over all initial states (J'', ν'') and summing over all final states (J', ν') . We obtain:

$$\alpha_{if}(T) = n_A n_B \frac{8\pi^3 \nu}{3c} \left(\frac{\hbar^2}{2\pi\mu k_B T}\right)^{3/2} \sum_{v',J',m'} \int_0^\infty \omega dK_i \exp\left(-\frac{\hbar^2 K_i^2}{2\mu k_B T}\right) |\langle f|er|i\rangle|^2 \rho_f(E'). \tag{1.49}$$

We can replaced the density of states $\rho_f(E')$ by the Dirac delta function [24].

$$\rho_f\left(E'\right) = \delta\left(h\nu - h\nu_{if}\right) \tag{1.50}$$

$$h\nu_{if} = E' - E'' + h\nu_0 \tag{1.51}$$

where ν_{if} and ν_0 are the specific transition frequencies between the considered molecular states and the atomic resonance frequency, respectively. while E' and E'' represent the energy of the bound and free states, in this order.

$$E'' = \epsilon'' \tag{1.52}$$

$$E' = E'_{v',J'} \tag{1.53}$$

By replacing the integral $\int d\mathbf{K}_i \delta\left(h\nu - h\nu_{if}\right)$ by the transformation [30].

$$\int \delta\left(h\nu - h\nu_{if}\right) d\mathbf{K}_i = \frac{1}{h} \int d\Omega \int K_i^2 \frac{dK_i}{d\nu} \delta\left(\nu - \nu_{if}\right) dv \tag{1.54}$$

$$= 4\pi \frac{K_i^2}{h} \frac{dK_i}{d\nu}\bigg|_{\nu=\nu_{if}} \tag{1.55}$$

The coefficient in (2.49) becomes

$$\alpha_{if}(T) = n_A n_B \frac{8\pi^3 \nu}{3c} \left(\frac{h^2}{2\pi\mu k_B T}\right)^{3/2} \sum_{v',J',m'} \int_0^\infty \omega \, 4\pi \frac{K_i^2}{h} \frac{dK_i}{d\nu}\bigg|_{\nu=\nu_{if}} \times \exp\left(-\frac{\hbar^2 K_i^2}{2\mu k_B T}\right) |\langle f| \, \mathrm{er} \, |i\rangle|^2 \rho_f \left(E'\right). \tag{1.56}$$

To evaluate the matrix element $\langle f|er|i\rangle$, we use equation (2.31) to obtain

$$\langle f|e\mathbf{r}|i\rangle = \langle \varphi'_N(\mathbf{R}) \, |\langle \varphi'_{el}(\mathbf{R},\mathbf{r})|e\mathbf{r}|\varphi''_{el}(\mathbf{R},\mathbf{r})\rangle| \, \varphi''_N(\mathbf{R})\rangle \tag{1.57}$$

$$= \langle \varphi'_N(\mathbf{R}) \, |\mathbf{D}_{if}(\mathbf{R})| \, \varphi''_N(\mathbf{R})\rangle \tag{1.58}$$

where $\mathbf{D}_{if}(\mathbf{R})$is the operator of the electronic transition dipole moment between the initial state $|i\rangle$ and the final state $|f\rangle$for each value of the inter-nuclear position vector R. It is defined by

$$\mathbf{D}_{if}(\mathbf{R}) = \langle \varphi'_{el}(\mathbf{R},\mathbf{r})|e\mathbf{r}|\varphi''_{el}(\mathbf{R},\mathbf{r})\rangle \, . \tag{1.59}$$

The operator $\mathbf{D}_{if}(\mathbf{R})$ in the situation of spherical symmetry is dependent on the distance R rather than the vector R's direction [30]. Next, we enter it in the form.

$$\mathbf{D}_{if}(\mathbf{R}) = D(R)\mathbf{u}_R \tag{1.60}$$

represents the unit vector in the direction of vector $\mathbf{R}$. According to (1.42), we can write

$$\begin{aligned}\varphi'_N(\mathbf{R}) &= \frac{\Psi_{J'}(R)}{R}\Upsilon^{m'}_{J'}(\theta,\Psi)\\ \varphi''_N(\mathbf{R}) &= \frac{\Psi_{J''}(R)}{R}\Upsilon^{m''}_{J''}(\theta,\Psi)\end{aligned} \tag{1.61}$$

Moreover, the wave function$\varphi''_N(\mathbf{R})$of the free states can be expanded in spherical harmonics along the axis carrying $\mathbf{K}_i$ [30].

$$\varphi''_N(\mathbf{R}) = \frac{\sqrt{4\pi}}{K_i R}\sum_{j''}(2j''+1)^{\frac{1}{2}}\, i^{j''}\exp\left(i\delta_{j''}\right)\Psi_{j''}(R)\Upsilon^0_{j''}(\theta,\Psi) \tag{1.62}$$

The absorption coefficient in equation (1.56) becomes

$$\begin{aligned}\alpha_{if}(T) &= n_A n_B \frac{8\pi^3\nu}{3c}\left(\frac{h^2}{2\pi\mu k_B T}\right)^{3/2}\\ &\times\sum_{v',J'}\sum_{m',J''}\omega\,(2J''+1)\,\frac{4\pi}{K_i^2}4\pi\frac{K_i^2}{h}\frac{dK_i}{d\nu}\bigg|_{\nu=\nu_{if}}\exp\left(-\frac{\hbar^2K_i^2}{2\mu k_B T}\right)\\ &\times\left|\int\Upsilon^{*0}_{J''}(\theta,\varphi)\mathbf{u}_R\Upsilon^{m'}_{J'}(\theta,\varphi)d\Omega\int_0^\infty\Psi_{J'}(R)D(R)\Psi_{J''}(R)dR\right|^2.\end{aligned} \tag{1.63}$$

On the right side of equation (1.63), the first integral accepts non-zero values only when $J''=J'\pm1$ $m'=0,\pm1$ [31]. The total of all J'' and m'' values is [30, 32].

$$\begin{aligned}\alpha^{\text{fb}}_{if} = 2n_An_B\frac{8\pi^3\nu}{3c}\left(\frac{h^2}{2\pi\mu k_BT}\right)^{3/2}&\sum_{v',J'}\omega\left(\frac{2\mu}{\hbar K_i^2}\right)\exp\left(-\frac{\hbar^2K_i^2}{2\mu k_BT}\right)\\ &\times\left[(J'+1)\left|\langle\Psi_{J'}(R)|D(R)|\Psi_{J'-1}(R)\rangle\right|^2\right.\\ &\left.+J'\left|\langle\Psi_{J'}(R)|D(R)|\Psi_{J'+1}(R)\rangle\right|^2\right]\end{aligned} \tag{1.64}$$

Given that the radial wave functions associated with the initial state adhere to energy normalization as delineated in equation (1.48), it is imperative to scale the second component of equation (1.64) by $\pi^2\frac{2K_i}{2\mu}$. Ultimately, the parameter of interest

becomes the diminished absorption coefficient f_b.

$$\alpha_r^{\mathrm{fb}} = \frac{\alpha_{if}^{\mathrm{fb}}}{n_A \cdot n_B} \tag{1.65}$$

at a given temperature T , between the initial free states (J'', ν'') and the final bound states (J', ν') is

$$\alpha_r^{f-b}(\nu, T) = \frac{8\Pi^3\nu}{3c}\pi \left(\frac{2\Pi^2\hbar^2}{\mu k_\beta T}\right)^{\frac{3}{2}} \sum_{\nu' J}(2J+1)\langle\Psi_{\nu'' J}|D(R)|\Psi_{\nu' J}\rangle^2 \exp -\frac{\epsilon''}{k_\beta T}. \tag{1.66}$$

where the solutions to the radial wave equation (1.46) for the free and bound states are represented by the wave functions $\Phi_{\nu'' J}$ and $\Phi_{\nu' J}$.

1.3.2 Free-Free transitions

For free-free (ff) transitions from the free state, which correspond to transitions from all lower free energy levels λ to all higher free energy levels (v) in continuous media [32], the decreased absorption coefficient α is provided at temperature T by:

$$\alpha_r^{f-f}(\nu, T) = \frac{8\Pi^3\nu}{3c}\varpi \left(\frac{2\Pi^2\hbar^2}{\mu k_\beta T}\right)^{\frac{3}{2}} \sum_{J}(2J+1) \int d\epsilon' \langle\varphi_{\epsilon'' J}|D(R)|\varphi_{\epsilon' J}\rangle^2 \exp -\frac{\epsilon''}{k_\beta T} \tag{1.67}$$

1.4 Photoemission Coefficient

In order to ascertain the photoemission profile, we take into account the free-free (f-f) and bound-free (b-f) transitions of the molecular states $\mathrm{A}^2\Pi_{1/2} \rightarrow \mathrm{X}^2\Sigma^+_{1/2}$

for the resonance line D1, and the two free-free (f-f) and bound-free (b-f) transitions corresponding to $A^2\Pi_{3/2} \rightarrow X^2\Sigma^+_{1/2}$ and the only free-free (f-f) transitions with regard to $B^2\Sigma^+_{1/2} \rightarrow X^2\Sigma^+_{1/2}$ for the resonance line D2.

1.4.1 Free-free Transition

we suggest that the reduced emission coefficient $k_r^{\mathrm{ff}}(\nu)$ for free-free transitions (ff) of molecular states $A^2\Pi_{1/2} \rightarrow X^2\Sigma^+_{1/2}$, $A^2\Pi_{3/2} \rightarrow X^2\Sigma^+_{1/2}$ and $B^2\Sigma^+_{1/2} \rightarrow X^2\Sigma^+_{1/2}$ could be expressed as follows [33, 34]

$$k_r^{\mathrm{ff}}(\nu) = \frac{64\pi^4\nu^3}{3hc^3}\omega\left(\frac{h^2}{2\pi\mu k_{\mathrm{B}}T}\right)^{3/2}\int_0^\infty d\epsilon_u \sum_J (2J+1)\left|\left\langle g_u^{\epsilon_u J}|D(R)|g_l^{\epsilon_l J}\right\rangle\right|^2 \exp\left(-\frac{\epsilon_u}{k_{\mathrm{B}}T}\right) \tag{1.68}$$

1.4.2 Free-bound Transition

The reduced emission coefficient $k_r^{\mathrm{fb}}(\nu)$ for **free-bound** transitions of states $A^2\Pi_{1/2} \rightarrow X^2\Sigma^+_{1/2}$ and $A^2\Pi_{3/2} \rightarrow X^2\Sigma^+_{1/2}$ is given by [35]

$$k_r^{\mathrm{bf}}(\nu) = \frac{64\pi^4\nu^3}{3hc^3}\omega\left(\frac{h^2}{2\pi\mu k_{\mathrm{B}}T}\right)^{3/2}\sum_{vJ}(2J+1)\left|\left\langle g_u^{vJ}|D(R)|g_l^{\epsilon_l J}\right\rangle\right|^2 \exp\left(-\frac{\epsilon_u}{k_{\mathrm{B}}T}\right). \tag{1.69}$$

Chapter 2:

Potentials Energy Curves and Transition Dipole Moments Construction

CHAPTER 2

POTENTIALS ENERGY CURVES AND TRANSITION DIPOLE MOMENTS CONSTRUCTION

This chapter is divided into two main parts: Potential Energy Curves (PECs) and Transition Dipole Moment (TDMs). The first part presents the method used to construct potential energy curves, V(R) of the RbAr system in both the ground and excited states for the two sets involved in the transitions. We use quantum chemistry methods, such as ab initio calculations, to predict the interaction potentials between the rubidium atom and the rare gas atom. The second part describes the method used to construct the transition dipole moments, $D(R)$, connecting the ground and excited molecular states of the RbAr dimer. This helps predict the probability of transitions between states.

2.1 EPCs Construction

In the domain of molecular calculations, interaction potentials $V(R)$ frequently exhibit an absence of precise analytical forms. To address this, the potentials are divided into three internuclear separation domains: the short region ($0 \leq R \leq R_s$), the intermediate region ($R_s \leq R \leq R_l$), and the long region ($R_l \leq R \leq \infty$). It is imperative to ascertain whether R_s, and R_l correspond to the internuclear site. The previous distances delimit the initial and terminal points of the intermediate region. To ensure a smooth and accurate connection between these domains, the cubic spline numerical interpolation method is employed. This

approach facilitates the construction of continuous and reliable potential energy curves, which are necessary for accurate calculations [36, 37].

2.1.1 Intermediate Region

The intermediate distance region, corresponding to $R_{RS} \leq R \leq R_{RL}$, is crucial because it allows us to construct potential energy curves for other regions. The data used here are either experimental or ab initio. Experimental data are obtained using the RKR method, developed by Rydberg, Klein, and Rees, which relies on spectroscopic measurements of diatomic molecules. This method involves numerically evaluating a pair of classical return points for each observed vibrational level. In contrast, ab initio values are derived from a quantum-theoretical approach to the molecular problem. Using the Born-Oppenheimer approximation, ab initio methods calculate the potential energy at specific values of R within a certain range of internuclear separations.

In the present study the generation of each potential energy curve was achieved by employing two distinct series of potential points, designated as set I and set II throughout this study. The initial set of data, henceforth referred to as set I, encompasses the reliable ab initio data points derived from Dhiflaoui et al [38].

The generation of these data is facilitated by a one-electron pseudo-potential approach, which incorporates the spin-orbit effect. This approach was first introduced by Barthelat et al [39], and has been employed in several prior computations [40–42]. It was contracted in which the Rb+ core and the effects of the electron-Ar interaction were substituted with a semilocal pseudo-potential. The

interaction between the electron and the Ar atom was modeled using a pseudopotential that had been previously employed in the examination of the Rydberg states of Ar_2 [43] excimers, Ar_3 clusters [44], and MAr (M = Li, Na, K) pairs [45], in addition to studies concerning the spectroscopic characteristics of atoms or molecules situated within Ar clusters or matrices [38]. For further specifics about the applied methodology, we direct the reader to reference [38].

The second data set, designated as Set II, consists of ab initio data points reported by Blank et al. [46], obtained through spin-orbit multi-reference configuration interaction (SO-MRCI) calculations. Is a high-level quantum chemical method particularly effective for systems where both electron correlation and relativistic spin-orbit effects play a crucial role. The approach combines two theoretical components:

Multi-Reference Configuration Interaction (MRCI):

In cases where a single-reference method (e.g., Hartree-Fock or coupled-cluster theory) is inadequate-such as near-degeneracies, bond dissociations, or excited states-MRCI provides a more accurate description. The wavefunction is constructed as a linear combination of several reference configurations, allowing electron correlation to be captured through excitations (typically single and double) from each reference state.

Spin-Orbit Coupling (SOC):

Originates from the interaction between an electron's spin and its orbital angular momentum. It becomes significant in heavy atoms and in excited-state

processes involving spin multiplicity changes (e.g., intersystem crossing). Accurate treatment of SOC is therefore essential for modeling fine-structure splittings, spectroscopy, and photophysical phenomena.

By integrating spin-orbit effects into the MRCI framework, SO-MRCI provides a balanced and reliable treatment of both static correlation and relativistic interactions. This makes it a valuable tool for studying potential energy surfaces, electronic spectra, and nonadiabatic processes in systems containing heavy atoms or transition metals [47, 48]. Some of the ab initio point values found by Dhflaoui [38] Blanck [46] are listed in Tables 1 and 2, and these are the values we used to generate our potential energy curves.

Distance	States			
R (a.u.)	$X^2\Sigma^+_{1/2}$	$A^2\Pi_{1/2}$	$A^2\Pi_{3/2}$	$B^2\Sigma^+_{1/2}$
3.00	/	0.9221	0.9289	0.9282
4.00	0.1637	0.2121	0.2136	0.2132
5.00	0.0268	0.0771	0.0779	0.0806
6.00	0.0049	0.0572	0.0580	0.0626
7.00	0.0011	0.0553	0.0560	0.0607
8.00	1.6102	0.0556	0.0563	0.0599
9.00	-1.4760	0.0559	0.0767	0.0588
10.00	-2.1393	0.0561	0.0569	0.0588
11.00	-1.9025	0.0561	0.0571	0.0580
12.00	-1.4421	0.0562	0.0572	0.0576
13.00	-1.0372	0.0562	0.0572	0.0574
14.00	-7.3550	0.0562	0.0573	0.0573
15.00	-5.2639	0.0562	0.0573	0.0573
16.00	-3.8650	0.0562	0.0573	0.0573
17.00	-2.8799	0.0562	0.0573	0.0573
20.00	-1.5710	0.0563	0.0574	0.0573

Table 1: A few potential energy values $V(R)$ for the ground states $X^2\Sigma^+_{1/2}$ and excited states $A^2\Pi_{1/2}$, $A^2\Pi_{3/2}$, and $B^2\Sigma^+_{1/2}$ of set I for the diatomic molecule RbAr

Distance	States			
R (a.u.)	$X^2\Sigma^+_{1/2}$	$A^2\Pi_{1/2}$	$A^2\Pi_{3/2}$	$B^2\Sigma^+_{1/2}$
3.00	0.79838	0.85641	0.85694	0.8732
4.00	0.1463	0.19705	0.19773	0.20077
5.00	0.02414	0.07484	0.07559	0.07958
6.00	0.00484	0.05739	0.05818	0.06391
7.00	0.00159	0.05617	0.05698	0.0629
8.00	5.223E-4	0.05656	0.05739	0.0622
9.00	1.820E-5	0.05688	0.05773	0.06103
10.00	-1.812E-4	0.05707	0.05793	0.05995
11.00	-2.232E-4	0.05717	0.05807	0.05919
12.00	-2.000E-4	0.05722	0.05816	0.05874
13.00	-1.578E-4	0.05724	0.05823	0.05851
14.00	-1.162E-4	0.05725	0.05828	0.05841
15.00	-8.258E-5	0.05726	0.05831	0.05837
16.00	-5.81E-5	0.05727	0.05834	0.05836
17.00	-4.10E-5	0.05728	0.05836	0.05836
20.00	-1.360E-5	0.0573	0.05838	0.05838

Table 2: A few potential energy values $V(R)$ for the ground states $X^2\Sigma^+_{1/2}$ and excited states $A^2\Pi_{1/2}$, $A^2\Pi_{3/2}$, and $B^2\Sigma^+_{1/2}$ of set II for the diatomic molecule RbAr

2.1.2 **Short Range**

In the short-range region, the interaction potentials are typically repulsive. This repulsion is caused by Coulomb forces when the electron clouds of two interacting atoms overlap closely [28]. At short distances, these interaction potentials change exponentially with R, following the form suggested by Born-Mayer [49].

$$V(R) = \alpha \exp -\beta R \tag{2.1}$$

The Born-Mayer constant parameters α and β, which require determination for each molecular state of RbAr, are crucial in the study. These parameters can be computed by utilizing the (2.2) relationships, assuming the continuity and familiarity of the potential V(R) and its derivatives at a specific point $R = Rs$. It has been established that R_S is equivalent to $3.25a_0$ for set I and $3.00a_0$ for set II, where A numerical approach, such as the cubic spline method, is employed to determine the derivative of V(R) at $R = Rs$. The values α and β obtained through this process are documented in table 3.

$$\begin{aligned} \alpha &= V\left(R_s\right) \exp\left(+\beta R_s\right), \\ \beta &= \frac{-1}{V\left(R_s\right)} \left(\frac{dV(R)}{dR}\right)_{R=R_s} \end{aligned} \tag{2.2}$$

Dissociation limit	Molecular states	Short range	
		α	β
$Rb(5s) + Ar(3s^2 3p^6)$	$X^2\Sigma^+_{1/2}$	103.470^a	1.6218^a
		114.596^b	1.61774^b
$Rb(5p) + Ar(3s^2 3p^6)$	$A^2\Pi_{1/2}$	109.235^a	1.63926^a
		78.1776^b	1.150104^b
	$A^2\Pi_{3/2}$	109.469^a	1.640211^a
		78.0559^b	1.49832^b
	$B^2\Sigma^+_{1/2}$	114.693^a	1.64903^a
		78.2695^b	1.49949^b

a: set I, b: set II.

Table 3: This table presents the potential parameters associated with the short-range interaction regions. All numerical values provided are expressed in atomic units.

2.1.3 **Long Range**

Here, specifically for $(R_l \leq R \leq \infty)$, the interactions between the electric dipole moments are the main reason why the potential is attractive. There are three different elements that contribute to these forces of contact at long distances when there is limited electronic overlap:

- Dispersive Forces: Also known as London forces, these arise from temporary fluctuations in the distribution of electric charge within molecules, leading to the creation of temporary dipoles that attract each other.

- Inductive Forces: These occur when the charge distribution in one molecule is influenced by the dipole in a neighboring molecule, resulting in an attractive

interaction between them.

- Electrostatic Forces: These result from the interaction between permanent electric dipoles in polar molecules [28, 50].

The potential in question may also be expressed as a sequence of inverse powers; this is also known as the van der Waals potential, and it is defined by the connection that follows.

$$V_{LR}(R) \backsim -\sum_{n} \frac{C_n}{R^n} \tag{2.3}$$

where the dispersion coefficients C_n are found in [37]. It is essential to remember that this analytical form can be used for distances larger than a certain value, known as the Le Roy radius and represented as $R > R_{LR}$ [51]. We shall take into consideration the first three coefficients for the sake of our task; thus, the connection becomes,

$$V(R) = -\frac{C_6}{R^6} - \frac{C_8}{R^8} - \frac{C_{10}}{R^{10}} \tag{2.4}$$

in this relation, the potential with the intermediate party is made in a way that is linear, $R = R_{LR}$ and the coefficients C_6, C_8, and C_{10} are tabulated in table 4.

Dissociation limit	Molecular states	Long range		
		C_6	C_8	C_{10}
$Rb(5s) + Ar(3s^2 3p^6)$	$X^2\Sigma^+_{1/2}$	336.4	$2.656.10^4$	$2.681.10^6$
$Rb(5p) + Ar(3s^2 3p^6)$	$A^2\Pi_{1/2}$	545.1	$1.403.10^4$	$1.066.10^6$
	$A^2\Pi_{3/2}$	545.1	$1.403.10^4$	$1.066.10^6$
	$B^2\Sigma^+_{1/2}$	924.2	$2.595.10^5$	$5.197.10^7$

Table 4: This table presents the potential parameters associated with the long-range interaction regions for set I and set II. The coefficients C_n are taken from the work of Mitroy and Zhang [37]. All numerical values provided are expressed in atomic units.

2.2 Potential Building

In particular, the construction of potential energy curves for each electronic state enables the detailed characterization of the nature of interactions in the RbAr systems. These curves provide insights into the binding energies, equilibrium distances and overall stability of the molecules. By analyzing and characterizing these potential energy curves, a deeper understanding of the physical and chemical properties of the RbAr systems can be gained.

2.3 Presentation of PECs

The potential energy curves that have been constructed are presented in Figure 1. This figure shows the potential curves corresponding to the $Rb(5s) + Ar(3s^2 3p^6)$, $Rb(5p_{1/2}) + Ar(3s^2 3p^6)$ and $Rb(5p_{3/2}) + Ar(3s^2 3p^6)$ two interactions for the RbAr system. As illustrated in Figure 1-a, set I is presented, while Figure 1-b illustrates set II.

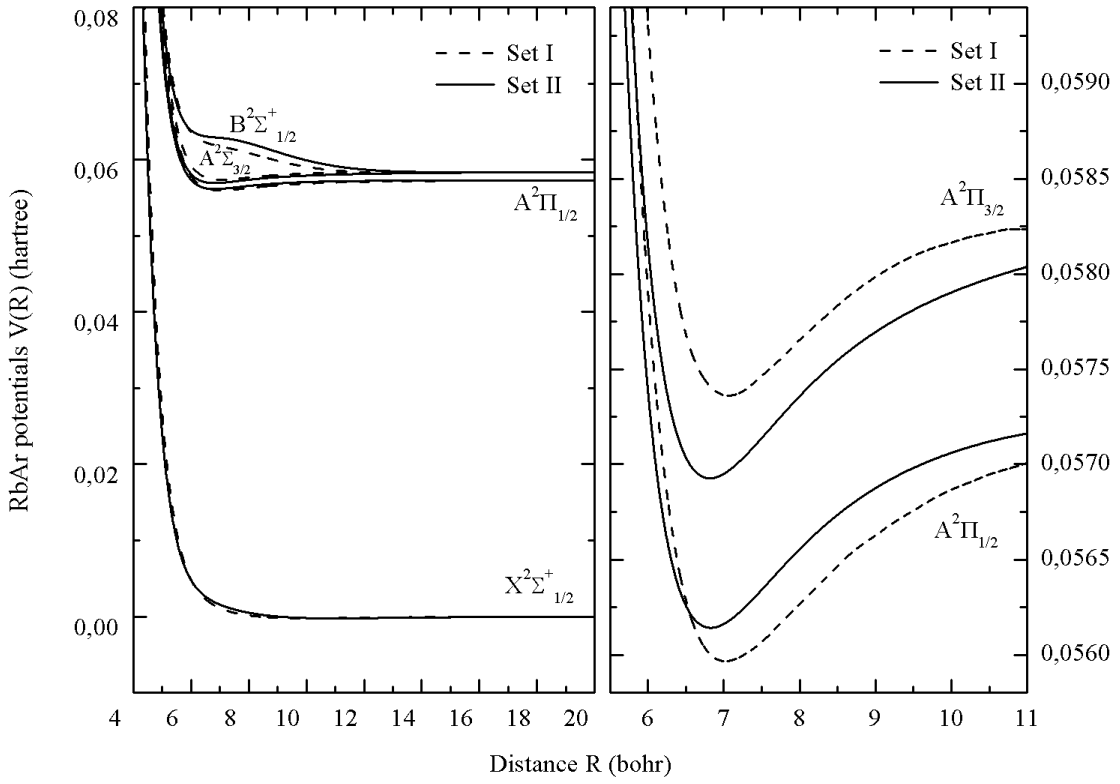

Figure 1: The developed RbAr potential energy curves and an expanded perspective of the $A^2\Pi_{1/2}$ and $A^2\Pi_{3/2}$ states.

2.4 Characterization of PECs

The potential energy curves can be characterized by determining a number of spectroscopic parameters, such as dissociation energies D_e, equilibrium positions, R_e and T_e the energy difference.

For this purpose we have summarized in Table 5 the spectroscopic parameters obtained by our constructions of the potential energy curves of the four molecular states for each set. In the same table we list those obtained by other authors for comparison.

Molecular slates	$D_e(cm^{-1})$	$R_e(A^\circ)$	$T_e(cm^{-1})$	Ref
$X^2\Sigma^+_{1/2}$	-47.0	5.30		set I
	-47.4590	5.807		set II
	-49.0	5.82		[46]
	-38.6	5.45		[52]
	-38.06	5.54		[53]
	-43.5	5.23		[54]
$A^2\Pi_{1/2}$	-224	3.74	12128	set I
	-253.750	3.605	13020.299	set II
	-255.2	3.60		[52]
	-238	3.59		[54]
$A^2\Pi_{3/2}$	-293	3.75	12296	set I
	-320.115	3.605	13086.664	set II
	-315.7	3.60		[52]
	-315.0	3.59		[54]
$B^2\Sigma^+_{1/2}$	-24.0	7.62	12565	set I
	-11.4292	8.590	12777.978	set II
	-7.3	8.57		[52]
	-11.9	8.25		[54]

Table 5: Comparison between the spectroscopic constants of the ground and excited RbAr potentials and the corresponding values reported in previous publications

2.5 Potential Differences

The potential energy difference curves between a ground state and an excited state are crucial for understanding the absorption spectrum, in semiclassical theory [16], the absorption spectrum reflects the transition probabilities between different energy states. When there is an extremum (a maximum or minimum) in the potential energy difference curve, it indicates a special point where the energy gap between the ground and excited states is either the largest or smallest.

This extremum creates what is known as a "satellite structure" in the absorption spectrum, an additional feature or peak that appears alongside the main

absorption line. By analyzing where this extremum occurs and converting it into the corresponding wavelength (λ), scientists can predict the precise location of the satellite in the absorption spectrum.

The presence of these satellite structures can provide valuable information about the electronic states of a molecule, the interactions between atoms, and the overall molecular dynamics. These details are essential for interpreting complex spectroscopic data, especially in systems where multiple states are involved.

According to the potential difference curves $V_{A^2\Pi_{1/2}-X^2\Sigma^+_{1/2}}(R)$, $V_{A^2\Pi_{3/2}-X^2\Sigma^+_{1/2}}(R)$, and $V_{B^2\Sigma^+_{1/2}-X^2\Sigma^+_{1/2}}(R)$ shown in Figure 3, there is a possibility of the appearance of a satellite in the blue wing for each set. This arises from the $B^2\Sigma^+_{1/2} \leftarrow X^2\Sigma^+_{1/2}$ transitions. For the set I, the satellite appears around $\lambda = 750$ nm, while for set II the satellite appears around $\lambda = 739$ nm shown in more detail in Figure 2. However, no satellite is classically predicted by the transitions $A^2\Pi_{1/2} \leftarrow X^2\Sigma^+_{1/2}$ and $A^2\Pi_{3/2} \leftarrow X^2\Sigma^+_{1/2}$.

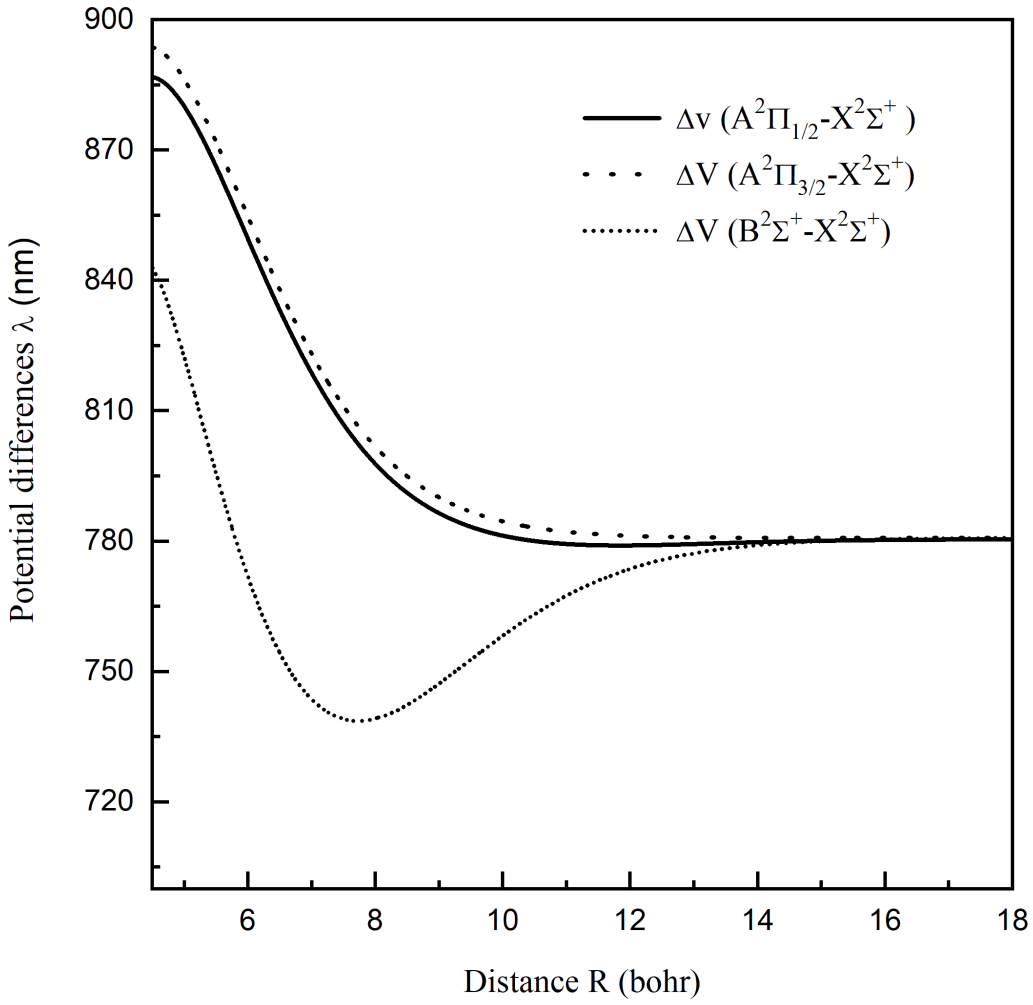

Figure 2: The differences between the potentials $V(B^2\,\Sigma_{1/2} - X^2\,\Sigma_{1/2})$, $V(A^2\,\Pi_{1/2} - X^2\,\Sigma_{1/2})$ and $V(A^2\,\Pi_{3/2} - X^2\,\Sigma_{1/2})$ for set II are shown as functions of the internuclear distance R.

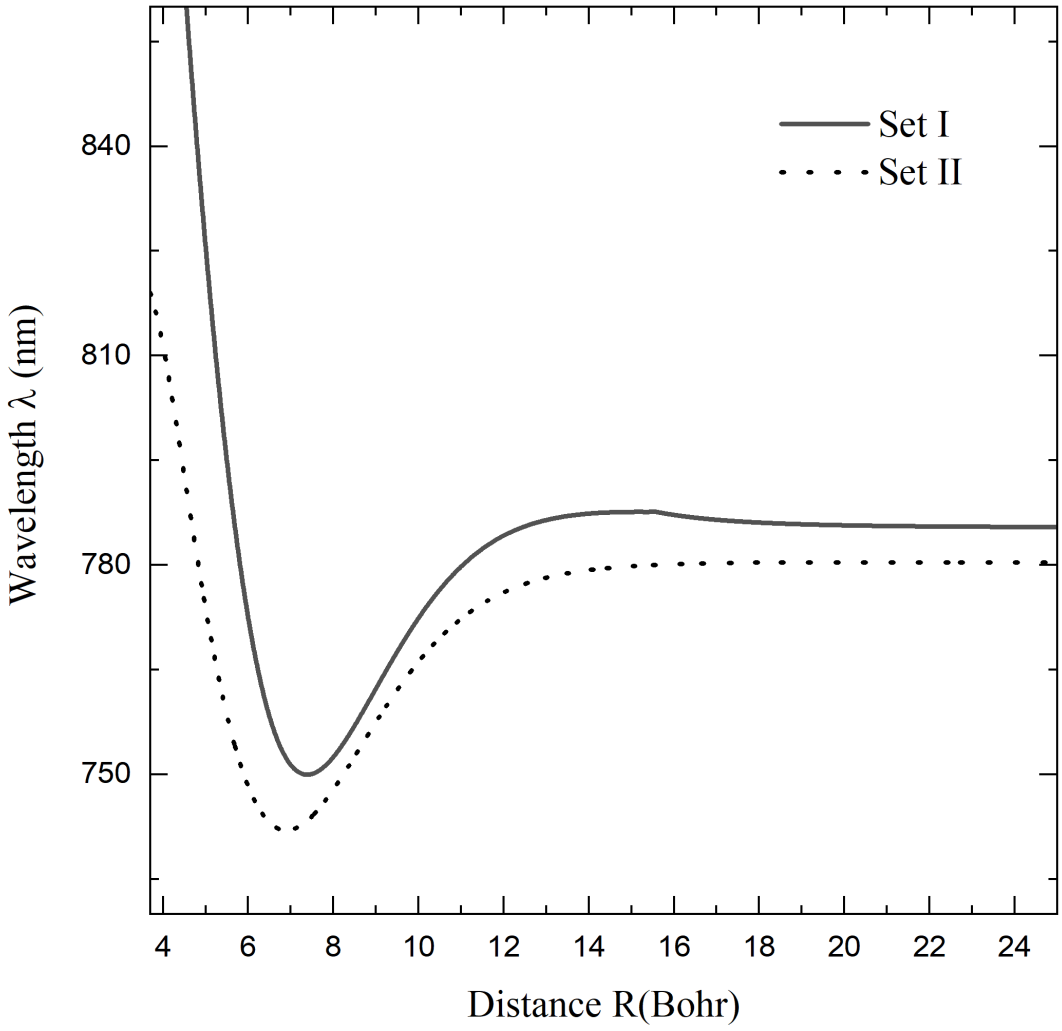

Figure 3: Differences in the potential energy curves $V(B^2\,\Sigma_{1/2} - X^2\,\Sigma_{1/2})$ are analyzed for both the set I and set II data sets, with the results represented in λ units.

2.6 Transition dipole moments TDMs

In our study, we construct the transition dipole moments (TDMs) using the same methodology applied to the potential energy curves. This involves generating the necessary curves across three distinct internuclear separation domains, denoted

as R. These domains cover different ranges of distances between the nuclei of the interacting atoms. To ensure accuracy and continuity, we smoothly connect the curves at the boundaries of these domains. This approach allows us to create a comprehensive and coherent representation of the TDMs over the entire range of internuclear separations.

2.6.1 The Intermediate Region

In the intermediate region, data points were obtained from a study by Blank et al [46]. These ab initio data points provide reliable values for transition dipole moments within the specified spatial range, indicating that these values are integral to our analysis and subsequent calculations.

2.6.2 The Long-Range Region

In the long-range region, the transition dipole moments (D(R)) exhibit a distinctive behavior that can be approximated using an asymptotic formula. This asymptotic formula is denoted as $D_L(R)$ and provides a mathematical framework for describing the dipole moments at large distances in the form [55]

$$D_L(R) \sim D_\infty + \alpha R^{-3} \tag{2.5}$$

In order to utilize this formula accurately, it is necessary to determine two parameters, designated as α and D_∞. The aforementioned parameters are established through a fitting process, which entails modifying the formula in a manner that aligns it with the long-range data, thereby ensuring that the calculated transition dipole moments are in close agreement with the observed data. The fitted values

for the parameters α and D_∞ are subsequently presented in Table 6, which contains the results of this fitting process.

Parameter	$D_{X^2\Sigma^+_{1/2}-A^2\Pi_{1/2}}$	$D_{X^2\Sigma^+_{1/2}-A^2\Pi_{1/2}}$	$D_{X^2\Sigma^+_{1/2}-B^2\Sigma^+_{1/2}}$
D_∞	7.28515	7.28482	7.28445
α	0.0040902	-3.91819	3.95674

Table 6: Fixed parameters were utilized for the established transition dipole moments in the long-range domain for set II datapoints.

2.6.3 The Short-Range Region

In the short-range region, the transition dipole moments (D(R)) display a distinct behavior compared to that observed in the long-range and intermediate regions. In this region, the dipole moments can be approximated by a linear form, denoted as $D_S(R)$. This indicates that, at short distances, the transition dipole moments increase or decrease in a linear fashion with respect to distance.

$$D_s(R) = A + bR \tag{2.6}$$

In this context, the parameters a and b are constant and are determined from the continuity condition of the TDM function and its first drift at the first data point, Rs.

2.7 Rotational-Vibrational Levels

The utmost vibrational and rotational quantum numbers, v and J, that each potential energy curve can support are also necessary for performing the necessary

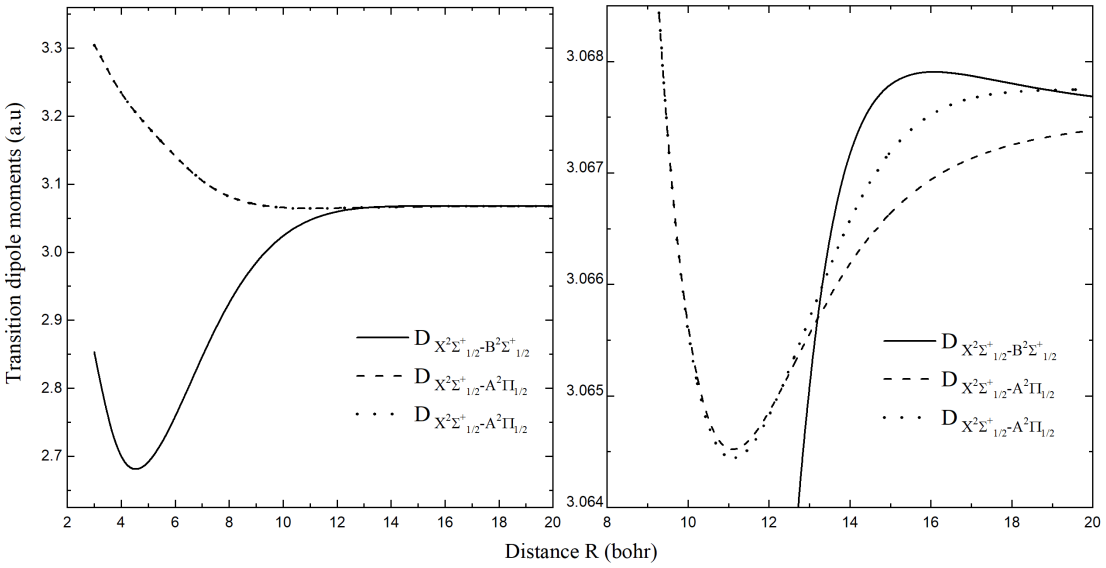

Figure 4: Transition dipole moments based on [46] data points.

numerical calculations, and it is important to recall the quantum treatment of the rotation and vibration of diatomic molecules. The rotational-vibrational energy $E(\nu, J) = E_{\nu,J}$ of a dimer is characterized by the vibration quantum number ν and the rotation quantum number J, both of which can take integer values. This energy is produced, in the context of diatomic molecule theory, by solving the radial wave equation numerically, using a recently developed form.

$$-\frac{\hbar^2}{2\mu}\frac{d^2}{dR^2}\Phi_{\nu,J}(R) + \left[V(R) + \frac{J(J+1)\hbar^2}{2\mu R^2}\right]\Phi_{\nu,J}(R) = E_{\nu,J}\Phi_{\nu,J}(R). \qquad (2.7)$$

By using this method, the generated potentials are guaranteed to be precise and dependable, offering a strong basis for additional spectrum analysis and associated research. When the diatom is in a generic situation where it is both rotating

and vibrating, the rotational-vibrational energy may be expressed as the sum of two terms.

$$E(\nu, J) = G(v, J = 0) + F_v(J)$$

where $F_v(J)$ the rotational energy is impacted by the vibration given as a power of $J(J+1)$ as [56] and $G(v, J = 0)$ is the vibration energy in the absence of rotation.

$$F_v(J) = B_v J(J+1) - D_v[J(J+1)]^2 + H_v[J(J+1)]^3 + \ldots$$

The B_v constant is an effective rotational constant that is dependent on ν and is associated with each vibration level. The centrifugal distortion constants are represented by $D_v, H_v \ldots$.

2.8 Rotationless Vibrational levels

In the context of non-rotational states, for a bound electronic state, the potential $V(R)$ has a minimum at the equilibrium distance R_e, defined by $V(R_e) = -D_e$. Here, D_e is the dissociation energy of the molecule, representing the depth of the potential well. To simplify the analysis of vibrational states around this equilibrium point, the potential can be expanded in a Taylor series in powers of $(R - R_e)$ around $R = R_e$. This expansion provides a more manageable form of the potential energy function for small displacements from the equilibrium distance, facilitating the study of molecular vibrations without considering rotational effects.

$$V(R) = -D_e + (R - R_e)\left(\frac{dV(R)}{dR}\right)_{R=R_e} + \frac{1}{2}(R - R_e)^2\left(\frac{d^2V(R)}{dR^2}\right)_{R=R_e} + \ldots$$

We will have if we stick to the second-order term.

$$V(R) = -D_e + \frac{1}{2}k\,(R - R_e)^2$$

$$k = d^2V(R)/\,dR^2\big|_{R=R_e}$$

The pure radial equation (2.1) becomes the equation of a harmonic oscillator if the diatom's rotation is negligible, or $J = 0$. The vibrational energy is then provided by [57].

$$G_{\text{vib}} = G(v, J = 0) = \hbar\omega_e \left(\nu + \frac{1}{2}\right),$$

where W_e is the vibration pulsation denoted by

$$\omega_e = \sqrt{\frac{k}{\mu}}$$

In the harmonic oscillator approximation, which is a simplified model used in quantum mechanics, the vibrational energy levels of a molecule are assumed to be equally spaced. Nevertheless, the potential curves of real molecules are anharmonic. As a consequence of this anharmonicity, the vibrational energy levels are not equally spaced. As the energy levels increase, the spacing between them decreases, indicating that the higher vibrational levels are more closely packed together. The higher levels are more closely packed together, and thus the vibrational energy can be more accurately described by a power series.

$$G_{\text{vib}} = \hbar\omega_e \left(\nu + \frac{1}{2}\right) - \omega_e x_e \left(\nu + \frac{1}{2}\right)^2 + \omega_e y_e \left(\nu + \frac{1}{2}\right)^3 + \ldots \tag{2.8}$$

with the initial anharmonicity coefficients being $\omega_e x_e$ and $\omega_e y_e$ [27] . Tables 7 and 8 present the detected rovibrational levels associated with $X^2\Sigma^+_{1/2}$ and excited states $A^2\Pi_{1/2}$, $A^2\Pi_{3/2}$, and $B^2\Sigma^+_{1/2}$ electronic states for Set I and Set II, corresponding to (J = 0) and (v = 0), respectively.

	$B^2\Sigma^+_{1/2}$		$A^2\Pi_{1/2}$		$A^2\Pi_{3/2}$		$X^2\Sigma^+_{1/2}$	
v	set I	set II	set I	set II	set I	set II	set I	set II
0	-52.0574	-55.4028	-186.5904	-223.2021	-188.3734	-222.9986	-40.6295	-43.6278
1	-46.2661	-44.3836	-153.0844	-187.6147	-155.0793	-185.8081	-32.6949	-36.3911
2	-39.4266	-34.4513	-123.6877	-155.6074	-124.4497	-153.1405	-25.8787	-29.7340
3	-32.7195	-26.3457	-97.1651	-127.0705	-96.8447	-123.9708	-19.3139	-23.6677
4	-25.9516	-19.3139	-73.3629	-101.8470	-71.4433	-97.8193	-13.9872	-18.2209
5	-19.9740	-13.5739	-52.5772	-79.7431	-49.1923	-74.7595	-9.5562	-13.4321
6	-14.7037	-9.6696	-34.8507	-60.5468	-29.4122	-54.4305	-6.0048	-9.3358
7	-10.2166	-5.6177	-20.7110	-44.0503	-11.5201	-36.5515	-3.2922	-5.9368
8	-6.7221	-3.1402	-10.5087	-30.0766		-20.8374	-1.4960	-3.1965
9	-4.0405	-1.5150	-6.2501	-18.5338		-7.1318	-0.4905	-1.1453
10	-2.1349	-0.5783	-2.8624	-9.5271			-0.0788	-0.2769
11	-0.9324	-0.1385		-3.5287				-0.0217
12	-0.2929	-0.0086		-0.3802				
13	-0.0436							

Table 7: Computed vibrational energy levels $E(v, J = 0)$ for the ground and excited RbAr molecular states, expressed in cm^{-1}, derived from sets I and II.

	$B^2\Sigma^+_{1/2}$		$A^2\Pi_{1/2}$		$A^2\Pi_{3/2}$		$X^2\Sigma^+_{1/2}$	
J	set I	set II	set I	set II	set I	set II	set I	set II
0	-40.6295	-43.6278	-186.5904	-223.2021	-188.3737	-296.3474	-52.0574	-55.3474
1	-40.5868	-43.5918	-186.0844	-223.1090	-188.0793	-296.8081	-52.0350	-55.6820
2	-40.5013	-43.519 8	-186.6877	-222.9230	-188.4497	-296.1405	-51.9901	-55.6402
3	-40.3732	-43.4119	-186.1651	-222.6440	-187.8447	-295.9708	-51.9227	-55.5776
4	-39.2024	-43.2681	-185.3629	-222.2720	-187.4433	-295.8193	-51.8327	-55.4942
5	-39.9889	-43.0885	-185.5772	-221. 8700	-187.1923	-294.7595	-51.7367	-55.3899
6	-39.7331	-42.8729	-184.8507	-221.2490	-186.4122	-294.4305	-51.5862	-55. 2647
7	-39.4347	-42.6217	-184.7110	-220.5983	-185.5201	-293.5515	-51.4292	-55.11186
8	-39.0940	-42.3347	-183.5087	-219.8946	-185.2156	-292.8374	-51.2500	-54.9518
9	-38.7111	-42.0121	-182.2501	-219.0183	-184.4265	-292.1318	-51.0484	-54.7640
10	-38.2860	-41.6540	-181.8624	-218.0193	-183.5501	-291.2143	-50.8246	-54.5555
20	-31.7501	-36.1466	-168.2812	-203.7193	-169.9937	-253.1757	-47.3719	-51.3268
30	-21.2730	-27.2676	-115.6801	-180.2067	-78.4379	-220.5749	-41.7585	-46.0294
40	-9.6411	-15.2985	-77.0446	-147.7486	-31.9267	-179.2732	-34.0724	-38.6833
50		-0.6765	-30.6775	-106.6421	-21.7637	-129.6841	-24.4167	-29.3148
60		+15.8961	+22.8348	-57.3143	+81.8093	-72.4006	-12.8922	-17.9551
70			+82.5665	-0.3842	+146.8613	-8.3156	-0.4158	-4.6406
80			+146.7730	+63.1965	+213.8593	+61.0159	-	+10.5868

Table 8: Computed rotational energy levels $E(v = 0, J)$ for the ground and excited RbAr molecular states, expressed in cm^{-1}, derived from sets I and II.

Chapter 3:

Results and Discussions

CHAPTER 3

RESULTS AND DISCUSSIONS

In order to evaluate the spectral profiles of rubidium broadened by rare gas atoms, it is necessary to study how these atoms produce spectral lines at specific wavelengths through their absorption and emission of light. The shapes of these lines are influenced by physical parameters such as temperature and density, which affect the motion and collision rates of the atoms. In addition, satellites, which appear as features on the sides of the main spectral lines, arise from interactions between atoms. The reduced absorption coefficients based on the two potential sets of RbAr systems are calculated by considering all transitions between the ground state and excited states with a frequency step size of 10 cm^{-1} for a temperature range from 500 to 3000 K. These calculations include both bound and quasi-bound energy levels and are performed across all relevant temperatures. For the rotational quantum number J, its maximum values are $J_{\max} = 250$ for free-free (ff) transitions and $J_{\max} = 20$ for free-bound (fb) transitions.

3.1 The Absorption Spectra

The absorption profiles occur around the D1 line at 794.8 nm, corresponding to the transition between the $X^2\Sigma^+_{1/2}$ ground state and the $A^2\Pi_{1/2}$ excited state of rubidium. Furthermore, the molecular ground and excited states are either repulsive or shallow. The transitions are therefore of the free-free or free-bound type.

Similarly, the D_2 line arises at 780.2 nm and corresponds to the transition from the $X^2\Sigma^+_{1/2}$ ground state to the $B^2\Sigma^+_{1/2}$ excited state. In this case as well, the relevant potential energy curves exhibit predominantly repulsive or shallowly bound character.

For reference to the resonance line labeled λ_{D1} in Figure 5, refer to the graph positioned on the rightmost side. the reduced absorption coefficients that $\alpha_r(\nu)$ are the result of the free-free and free-bound $X^2\Sigma^+_{1/2} \rightarrow A^2\Pi_{1/2}$ transitions. This is because the ground state $X^2\Sigma^+_{1/2}$ is repulsive, while the excited state $A^2\Pi_{1/2}$ is very shallow. As a result, both free-free (f-f) and free-bound (f-b) transitions occur, indicating that the interactions are either weakly bound or entirely unbound.

For the resonance line labeled λ_{D2} which is displayed in Figure 5 (see the left graph), the far wings that arise from the $X^2\Sigma^+_{1/2} \rightarrow A^2\Pi_{3/2}$ transitions are also of the free-free (f-f) and free-bound (f-b) types. The $X^2\Sigma^+_{1/2} \rightarrow B^2\Sigma^+_{1/2}$ transition is exclusively free-free (f-f) because the $A^2\Pi_{3/2}$ state is not deep enough, and the $B^2\Sigma^+_{1/2}$ state is completely repulsive. These characteristics result in distinctive absorption profiles in the two sets of RbAr systems, with transitions extending far beyond the central wavelengths due to the shallow and repulsive nature of the involved states.

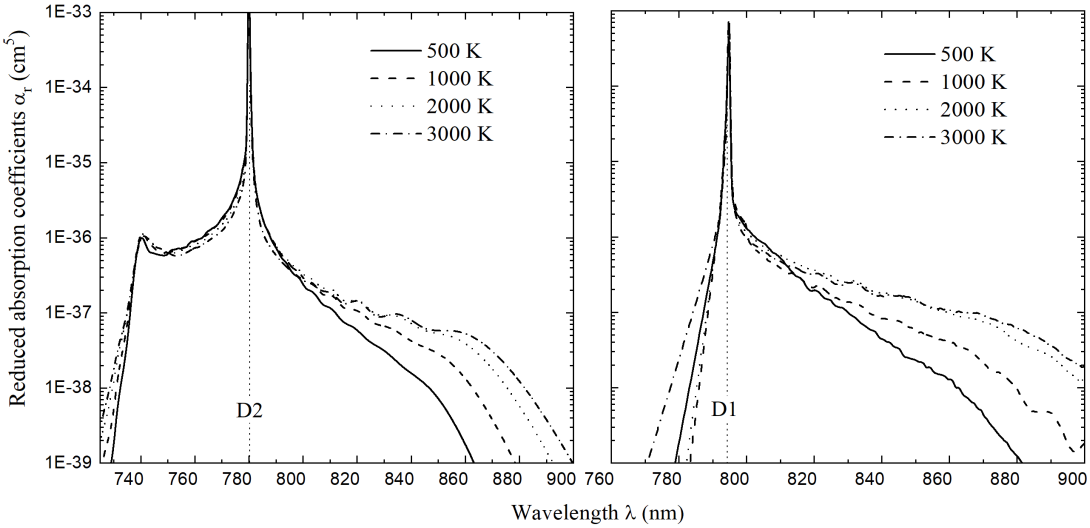

Figure 5: The effect of temperature on the photoabsorption profiles around the D1 and D2 lines, as computed using the set II potential.

Figure 6 illustrates the fully quantum mechanical RbAr photoabsorption spectra computed at 1000 K using interatomic potential sets I and II. Figures 6(a) and 6(b) present the spectral region around the D_1 wavelength $\lambda_{D1} = 794.8$ nm, which originates from the free-free and free-bound $X^2\Sigma^+_{1/2} \rightarrow A^2\Pi_{1/2}$ transitions. The simulations indicate that the free-bound contributions are negligible in comparison with the free-free ones. The resulting spectra show a pronounced red wing and rapidly diminish on the blue side.

Figures 6(c) and 6(d) present the absorption spectra in the vicinity of $\lambda_2 = 780.0$ nm. These profiles represent the combined contributions of the $X^2\Sigma^+_{1/2} \rightarrow A^2\Pi_{3/2}$ and $X^2\Sigma^+_{1/2} \rightarrow B^2\Sigma^+_{1/2}$ transitions. In this wavelength region, the calculation includes the free–free transitions $X^2\Sigma^+_{1/2} \rightarrow A^2\Pi_{1/2}$ and $X^2\Sigma^+_{1/2} \rightarrow B^2\Sigma^+_{1/2}$, together with the free-bound transitions to the $A^2\Pi_{3/2}$ state. Regardless of whether

the first or second potential set is used, the broadened D_2 line exhibits both blue and red wings, with a distinct satellite feature emerging in the far-blue wing. The blue wing and its associated satellite originate from the $X^2\Sigma^+_{1/2} \rightarrow B^2\Sigma^+_{1/2}$ transition, whereas the red wing is mainly due to the $X^2\Sigma^+_{1/2} \rightarrow A^2\Pi_{1/2}$ transition, as illustrated in Figures 6(e) and 6(f). The inset of the same figure highlights the free-free and free-bound contributions to the $X^2\Sigma^+_{1/2} \rightarrow A^2\Pi_{3/2}$ transition, clearly showing that the free-bound component is significantly weaker than the free-free one. The absorption profiles of the broadened D_1 and D_2 lines are dominated by free-free (f-f) transitions across the entire temperature range, as the contributions from free-bound (f-b) transitions are negligible in comparison. Figure 7 presents a total profile of the broadened D_1 and D_2line of set II, covering the wavelength range from 500 to 900 nm for the temperature [500, 1000, 2000, and 3000 K]. The overall spectral shape, as well as the position and amplitude of the satellite feature, remains essentially unchanged across this temperature interval. However, the intensity of the far-red wing increases noticeably with increasing temperature.

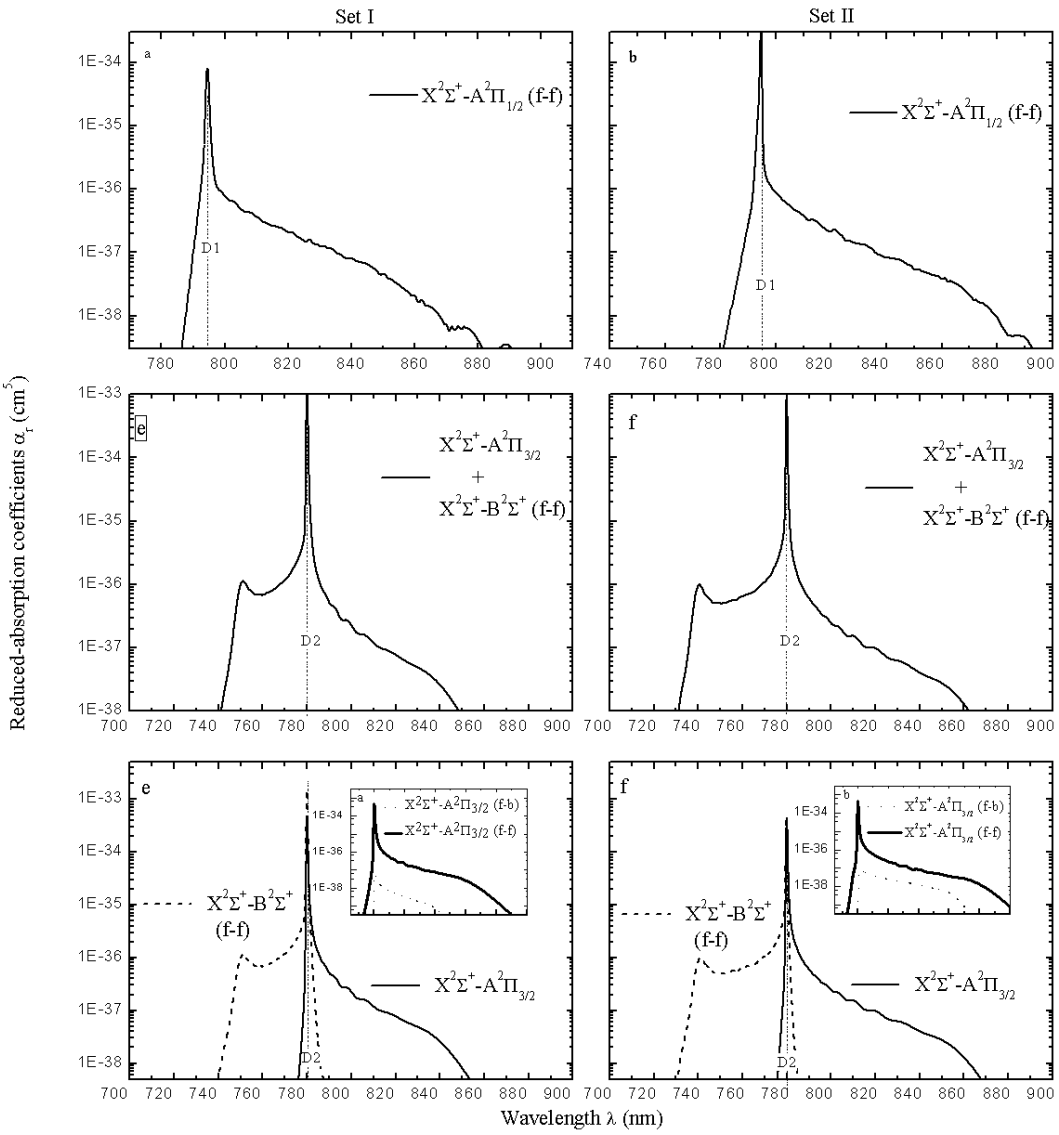

Figure 6: The reduced RbAr photoabsorption coefficients computed at 1000 K using potential sets I and II are presented. The vertical dash-dotted lines indicate the wavelengths of the unperturbed atomic rubidium transitions

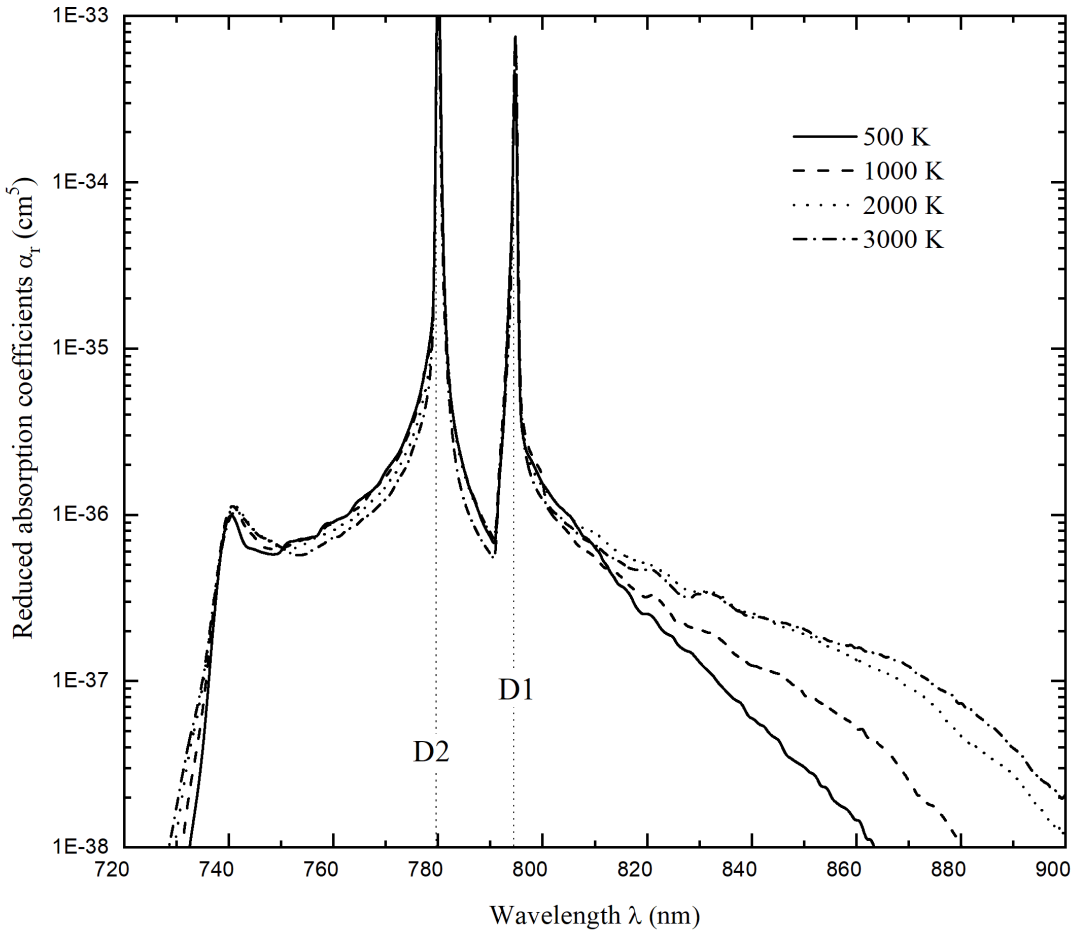

Figure 7: The influence of temperature on the overall photoabsorption profiles, as calculated using the set II potential.

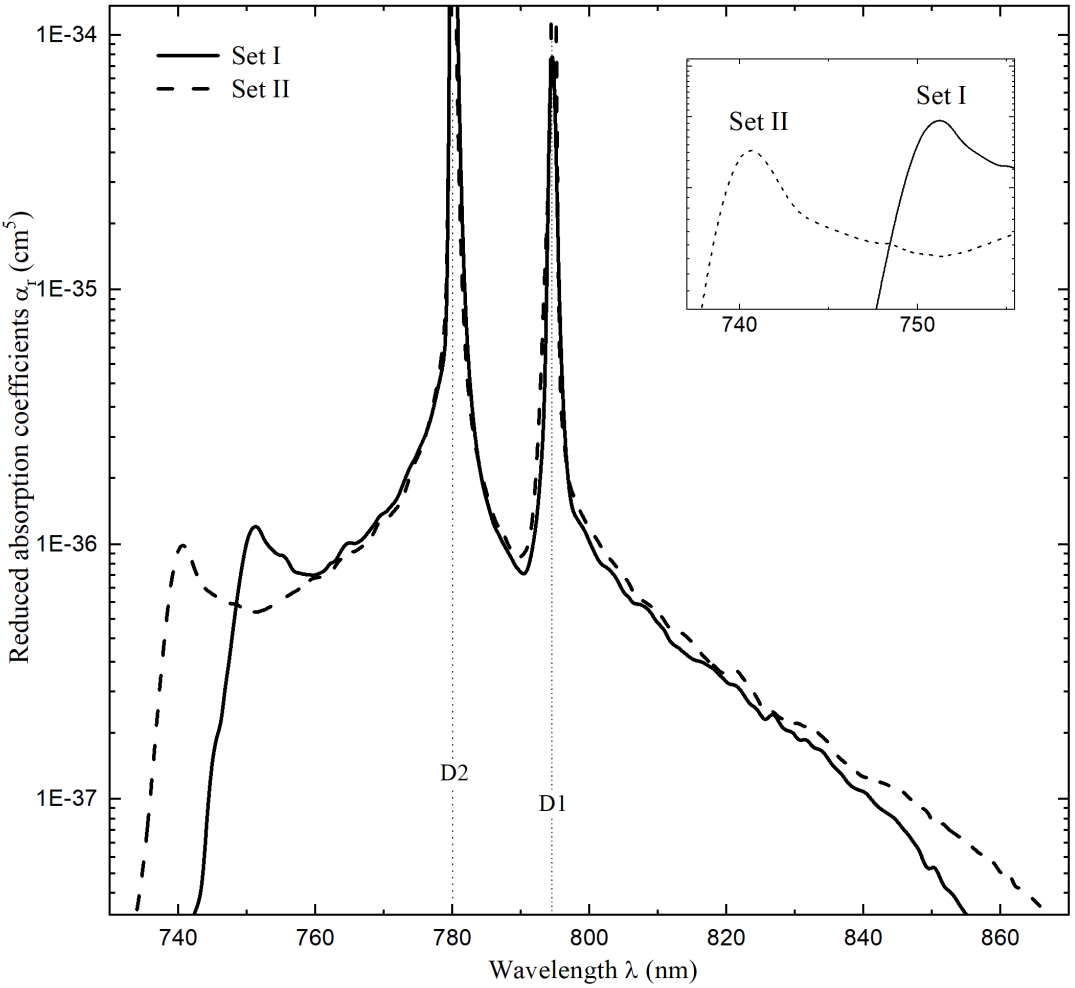

Figure 8: A comparison of the reduced photoabsorption coefficients of RbAr at 1000 K calculated using the set I and set II potentials. The inset shows the positions and intensities of the satellite features corresponding to calculations based on both sets of potentials.

In Figure 8, the solid and dashed curves correspond to absorption spectra calculated by using the first and second sets of potential data, respectively. Although the two spectra exhibit similar overall shapes, the associated satellite features appear at different wavelengths: $\lambda_1 = 750$ nm when employing the set I potentials and

$\lambda_2 = 740$ nm when using set II. This noticeable shift in the satellite positions is most likely attributable to differences in the underlying interatomic potentials, which are themselves highly sensitive to the basis set used in generating the potential energy points. According to classical considerations, the location of such satellites can be inferred from the differences between the relevant potential energy curves. For this reason, we have plotted in Figure 3 in chapter 2 the potential difference $V(\mathrm{B}^2\Sigma^+_{1/2}) - V(\mathrm{X}^2\Sigma^+_{1/2})$, expressed in terms of wavelength. As expected, the two resulting curves exhibit extrema at $\lambda_1 = 749.99$ nm for set I and $\lambda_2 = 742.01$ nm for set II. These extrema are in good agreement with the satellite positions extracted from the corresponding spectra. A comparable satellite near 750 nm has previously been reported in the experiments of Moroshkin et al. [12], Rice et al. [13], and Ockenfels et al. [14], in full consistency with the value obtained using the set I potentials.

In addition, we have recalculated the $\mathrm{X}^2\Sigma^+_{1/2} - \mathrm{B}^2\Sigma^+_{1/2}$ photoabsorption spectrum using the potential data of Dhiflaoui et al. [38], which do not incorporate spin-orbit coupling. These potentials were generated using the same computational method as that employed for the set I data. The resulting profile, shown in Figure 9, closely matches the spectrum obtained from set I, and the satellite feature again appears at $\lambda_1 \approx 750$ nm.

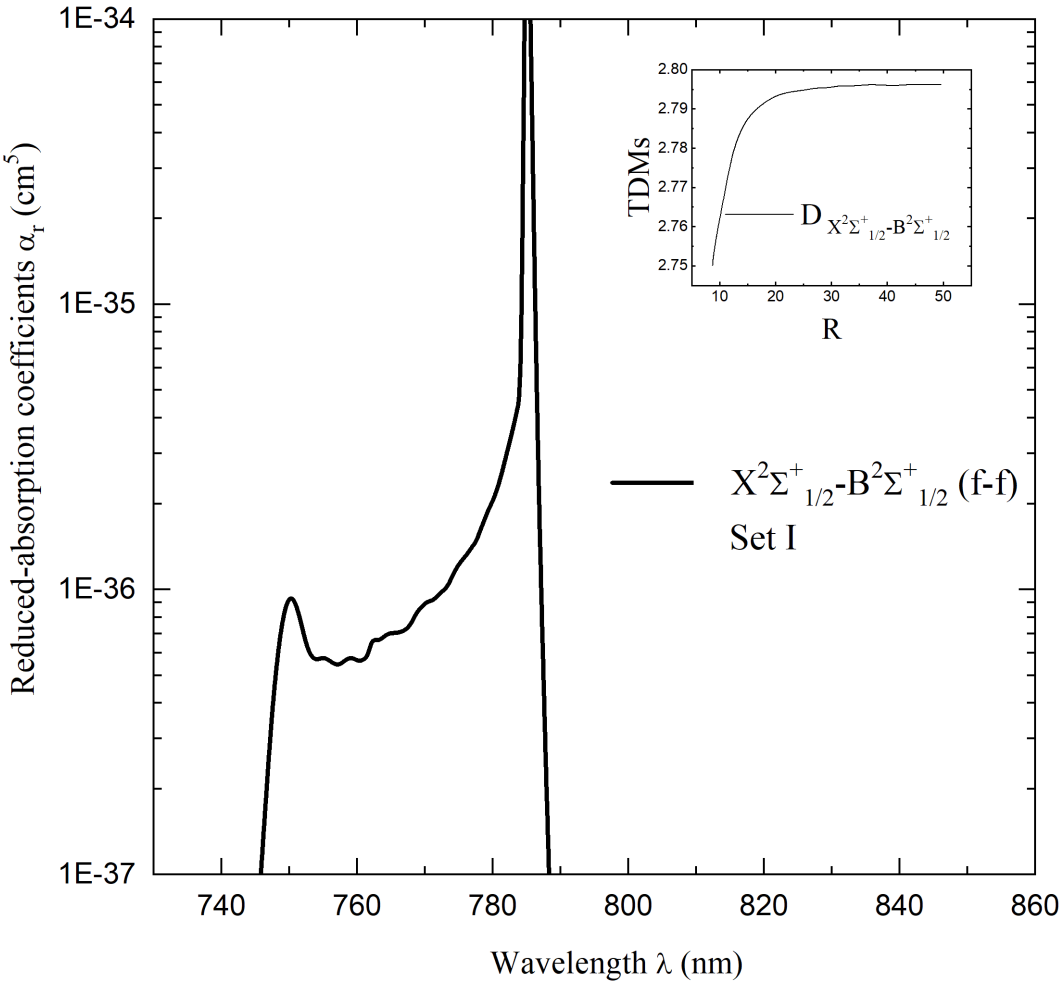

Figure 9: Reduced photo-absorption coefficients corresponding to $X^2\Sigma^+_{1/2} - B^2\Sigma^+_{1/2}$ transitions when the calculations are based on the potentials without including the spin-orbit effect. The inset shows the RbAr ($X^2\Sigma^+_{1/2} - B^2\Sigma^+_{1/2}$) dipole moments from Dhiflaoui et al. [38].

3.2 The Emission Spectra

It is important to note that, similar to the absorption profiles of the RbAr diatomic system computations, the free boundary and free-free (ff) transitions similarly enhance the emission spectra of the D1 and D2 resonance lines. In our analysis, we have considered a number of transitions between the relevant molecular states, as outlined below: In the case of the D_1 resonance line, two distinct types of transitions are considered: free-free transitions refer to transitions involving the molecular states, X $^2\Sigma^+_{1/2} \leftarrow$ A $^2\Pi_{1/2}$ and free-bound transitions, also refer to transitions between the molecular states X $^2\Sigma^+_{1/2} \leftarrow$ A $^2\Pi_{1/2}$.

In considering the D_2 resonance line, the following factors are taken into account: free-free transitions, whereby transitions occur between the states A $^2\Pi_{3/2} \rightarrow$ X $^2\Sigma^+_{1/2}$, free-bound transitions, also concerning transitions from A $^2\Pi_{3/2} \rightarrow$ X $^2\Sigma^+_{1/2}$ and free-free transitions only for the transitions X $^2\Sigma^+_{1/2} \leftarrow$ B $^2\Sigma^+_{1/2}$, where only free-free transitions are considered. By considering these transitions, the photo-emission profile can be studied to set the position of the blue satellite. The overall appearance of the emission spectra closely follows that of the absorption profiles. Specifically, the D1 line displays only a red wing, whereas the D2 line exhibits both red and blue wings, in addition to a satellite feature located near $\lambda_1 = 750\ nm$ when using the set I potentials and around $\lambda_2 = 740\ nm$ with set II. These positions are consistent with the satellite structures observed in the absorption spectra. Furthermore, Figures 10(e) and 10(f) show that the blue wing of the D2 line originates from the X $^2\Sigma^+_{1/2} \leftarrow$ B $^2\Sigma^+_{1/2}$ transition, including the satellite contribution, while the red

wing is associated with the X $^2\Sigma^+_{1/2} \leftarrow$ A $^2\Pi_{3/2}$ transitions. It is also worth noting that, unlike the absorption case, the satellite amplitude increases substantially as the temperature rises from 500 to 1000 K, with the feature based on set II being more sensitive to this change. Overall, the full quantum calculations successfully reproduce the experimentally measured absorption and emission profiles reported in Ref. [12–14]. .

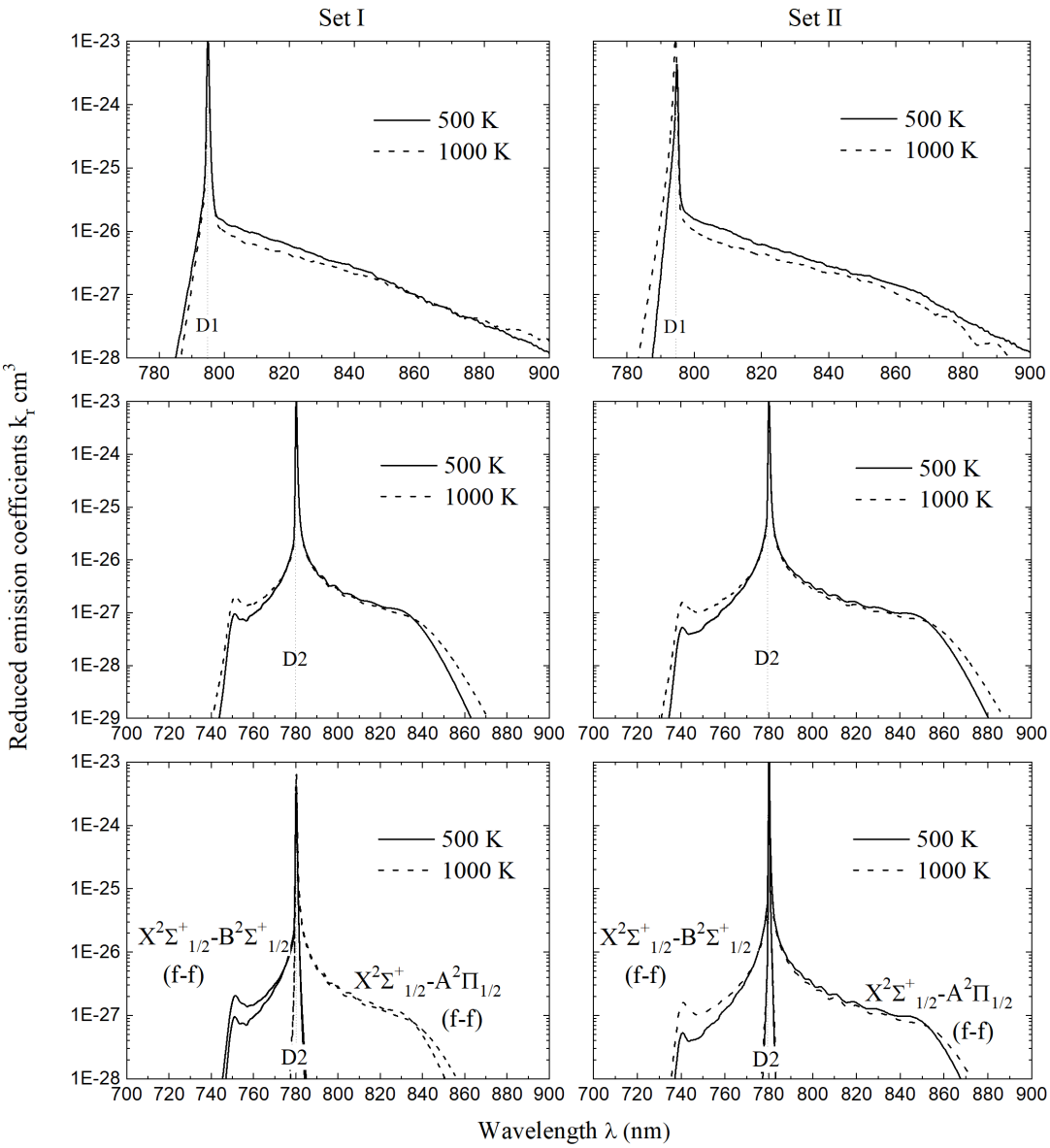

Figure 10: Reduced photoemission coefficients of RbAr at 500 K and 1000 K, computed using both set I and set II potentials.

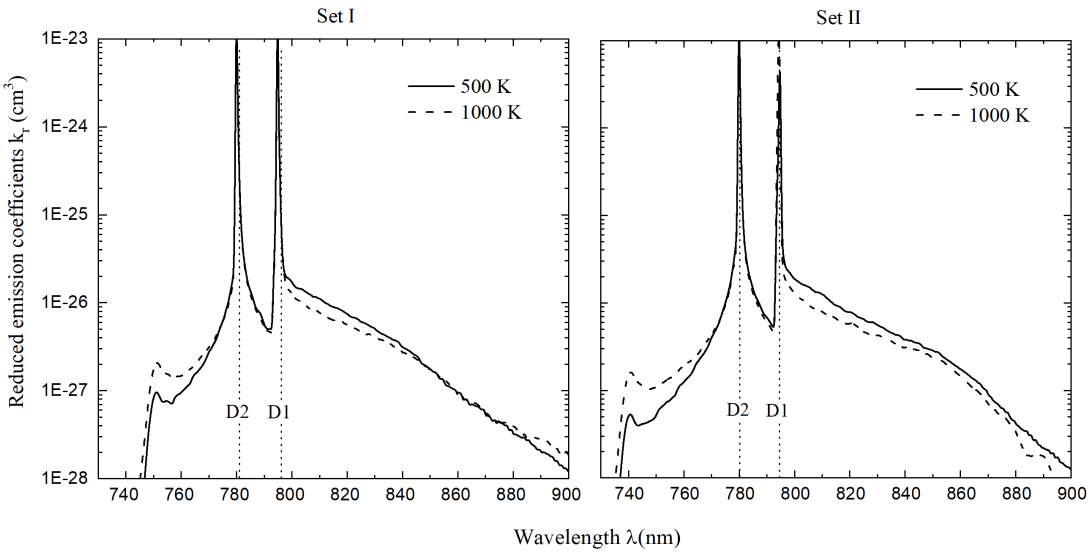

Figure 11: Total reduced photoemission coefficients of RbAr at 500 K and 1000 K, calculated using both set I and set II potentials.

3.3 Comparison

A comparison between our calculated satellite positions and the values reported in the literature shows a consistent alignment across different data sources. Using both potential sets (set I and set II), the present work predicts blue-shifted satellite features at approximately 750 nm and 740 nm, respectively. These theoretical estimates fall within the range of experimental measurements available for the RbAr system, which cluster around 736-755 nm, as reported by Ralchenko et al., Carrington et al., Goll et al., and Ockenfels et al. Although slight deviations are observed for instance, the set II value lies closer to the lower experimental limit, while the set I value approaches the upper range the overall agreement highlights the reliability of the calculated extrema of the difference potentials $B^2\Sigma^+_{1/2} - X^2\Sigma^+_{1/2}$

This concordance reinforces the physical consistency of our model and confirms that both potential sets capture the correct spectral behavior of the blue-shifted satellite; all previously mentioned data are displayed in table 8.

System	satellites $\lambda(nm)$					
	This work		Theo	Exp	Exp	Exp
	set I	set II	[58]	[59]	[52]	[14]
RbAr	750	740	736.2	755.5	754	754

Table 9: The experimental and theoretical locations (in nanometers) of blue-shifted satellites are compared to the results of set I and set II positions of satellites .

With respect to the comparison with previously reported theoretical studies, it should be noted that the only RbAr absorption and emission spectra available in the literature are those computed by Moroshkin and his co-workers [12] within the framework of the unified line-shape theory [60–62]. Their calculations were carried out at a temperature of 400 K and relied on the potential energy curves published in Ref. [38]. To enable a meaningful comparison, we generated our own quantum-mechanical RbAr absorption and emission profiles at the same temperature (400 K), using the same set of potentials; these results are presented in Figure 12. The comparison reveals that, although both approaches predict similar global spectral features, the classical treatment used in Ref. [12] is unable to reproduce a key characteristic of the spectra namely, the blue satellite structure that is clearly present in our quantum simulations and is also confirmed experimentally. This

discrepancy highlights the importance of a fully quantum description for accurately capturing such subtle spectral features.

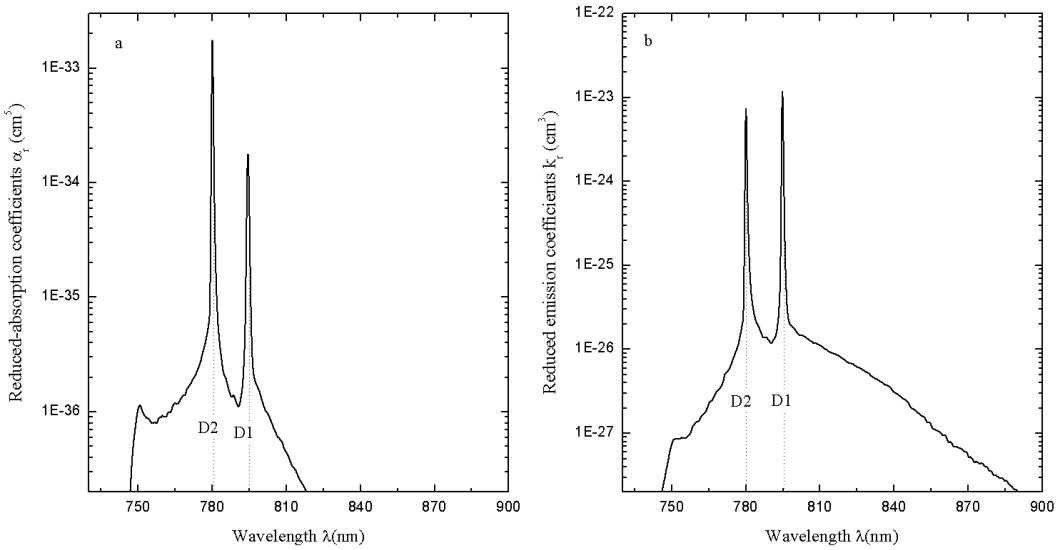

Figure 12: Part a is the reduced photoabsorption and part b represents the reduced emission spectra of RbAr, both computed at 400 K using the set I potentials.

Conclusion

In conclusion, this thesis provides a quantum study of the absorption and emission spectrum of rubidium (Rb) atoms, specifically perturbed by collisions with argon (Ar) atoms. The investigation covers a temperature range from 500 to 3000 Kelvin, focusing on the far wings of D_1 and D_2 resonance lines of the rubidium atom, influenced by the presence of Ar atoms in both absorption and emission phenomena within the wavelength range of 500-900 nm.

The research began with the construction of electronic potential energy curves for the ground state $X^2\Sigma^+_{1/2}$ and excited states $A^2\Pi_{1/2}$, $A^2\Pi_{3/2}$ and $B^2\Sigma^+_{1/2}$ of the RbAr dimer and the corresponding transition dipole moments as a function of internuclear distance (R). These calculations were performed using two sets of ab initio data points. Important spectroscopic parameters were calculated to characterize the potential energy curves, including the equilibrium position R_e, well depth D_e, and energy differential T_e, as well as the rotational-vibrational levels of the excited states $A^2\Pi_{1/2}$, $A^2\Pi_{3/2}$ and $B^2\Sigma^+_{1/2}$, all of them were calculated and compared with previous experimental and theoretical results.

Subsequent to the preliminary calculations, the absorption and emission coefficients within the wavelength range of [500-900 nm] at varying temperatures were ascertained for the two sets of potential data. The study successfully identified a satellite in the blue wing of the absorption spectra resulting from free-free transitions between the X and B states, with wavelengths of approximately 750 nm for set I and 740 nm for set II. These findings agree with previous theoretical and experimental results.

References

REFERENCE LIST

[1] J. Readle, J. Eden, J. Verdeyen, and D. Carroll, *Applied Physics Letters*, vol. 97, no. 021104, (2010).

[2] J. Readle, J. Verdeyen, J. Eden, S. Davis, K. Galbally-Kinney, W. Rawlins, and W. Kessler, *Optics letters*, vol. 34, no. 23, pp. 3638–3640, (2009).

[3] J. Readle, C. Wagner, J. Verdeyen, D. Carroll, and J. Eden, *Electronics Letters*, vol. 44, no. 25, pp. 1466–1467, (2008).

[4] J. Hewitt, T. Houlahan, J. E. Gallagher, D. Carroll, A. Palla, J. Verdeyen, G. P. Perram, and J. Eden, *Applied Physics Letters*, vol. 102, no. 111104, (2013).

[5] N. D. Zameroski, G. D. Hager, W. Rudolph, and D. A. Hostutler, *Journal of the Optical Society of America B*, vol. 28, no. 5, pp. 1088–1099, (2011).

[6] N. Allard, F. Allard, P. Hauschildt, J. Kielkopf, and L. Machin, *Astronomy & Astrophysics*, vol. 411, no. 3, pp. L473–L476, (2003).

[7] A. Burrows and M. Volobuyev, *The Astrophysical Journal*, vol. 583, no. 2, p. 985, (2003).

[8] D. Drummond and A. Gallagher, *The Journal of Chemical Physics*, vol. 60, no. 9, pp. 3426–3435, (19740.

[9] I. Dubourg, M. Ferray, J. Visticot, and B. Sayer, *Journal of Physics B: Atomic and Molecular Physics*, vol. 19, no. 8, p. 1165, (1986).

[10] R. D. Loper and D. E. Weeks, *Journal of Physics B: Atomic, Molecular and Optical Physics*, vol. 53, no. 20, p. 205403, (2020).

[11] L.-C. Ha, X. Zhang, N. Dao, and K. R. Overstreet, *Physical Review A*, vol. 103, no. 2, p. 022826, (2021).

[12] P. Moroshkin, L. Weller, A. Saß, J. Klaers, and M. Weitz, *Physical review letters*, vol. 113, no. 6, p. 063002, (2014).

[13] C. A. Rice, K. Lapp, A. Rapp, W. S. Miller, and G. P. Perram, *Journal of Quantitative Spectroscopy and Radiative Transfer*, vol. 224, pp. 550–555, (2019).

[14] T. Ockenfels, P. Roje, T. vom Hövel, F. Vewinger, and M. Weitz, *Physical Review A*, vol. 106, no. 1, p. 012815, 2022.

[15] N. Allard and J. Kielkopf, *Reviews of modern physics*, vol. 54, no. 4, p. 1103, 1982.

[16] J. Szudy and W. E. Baylis, *Physics reports*, vol. 266, no. 3-4, pp. 127–227, 1996.

[17] F. Shindo, J. F. Babb, K. Kirby, and K. Yoshino, *Journal of Physics B: Atomic, Molecular and Optical Physics*, vol. 40, no. 14, p. 2841, 2007.

[18] W. Hindmarsh and J. M. Farr, *Journal of Physics B: Atomic and Molecular Physics*, vol. 2, no. 12, p. 1388, 1969.

[19] W. Hindmarsh and J. M. Rarr, *Journal of Physics B: Atomic and Molecular Physics*, vol. 2, no. 12, p. 1388, 1969.

[20] K. Alioua and M. Bouledroua, *Physical Review AâAtomic, Molecular, and Optical Physics*, vol. 74, no. 3, p. 032711, 2006.

[21] P. Côté, R. O. Marzke, M. J. West, and D. Minniti, "Evidence for the hierarchical formation of thegalactic spheroid," *The Astrophysical Journal*, vol. 533, no. 2, p. 869, 2000.

[22] H. Friedrich and H. Friedrich. Springer, 2006, vol. 3.

[23] S. Rajasekar and R. Velusamy, *Quantum Mechanics I: The Fundamentals*. CRC Press, 2022.

[24] B. H. Bransden and C. J. Joachain. Pearson Education India, 2003.

[25] J. D. Jackson. John Wiley & Sons, 2021.

[26] F. Reif, *Fundamentals of Statistical and Thermal Physics, (McGraw-Hill Book Co.,New York, 1965).*, Tokyo.

[27] G. Herzberg, *Molecular Spectra and Molecular Structure, Vol. I : Spectra of Diatomic Molecules, (D.Van Nostrand Co., Princeton, 1963).*

[28] J. O. Hirschfelder, C. F. Curtis, and R. B. Bird, New York, 1954.

[29] *Handbook of Mathematical Functions*. New York: Dover, 1965.

[30] R. O. Doyle, *Journal of Quantitative Spectroscopy and Radiative Transfer*, vol. 8, no. 9, pp. 1555–1569, 1968.

[31] E. L. Durand. Paris : Masson, 1970.

[32] K. Sando and A. Dalgarno, *Molecular Physics*, vol. 20, no. 1, pp. 103–112, 1971.

[33] P. Herman and K. Sando, *The Journal of Chemical Physics*, vol. 68, no. 3, pp. 1153–1160, 1978.

[34] K. Sando, *Molecular Physics*, vol. 21, no. 3, pp. 439–447, 1971.

[35] J. Woerdman, J. Schlejen, J. Korving, M. van Hemert, J. de Groot, and R. van Hal, *Journal of Physics B: Atomic and Molecular Physics*, vol. 18, no. 21, p. 4205, 1985.

[36] W. H. Press, B. P. Flannery, S. A. Teukolsky, and W. T. Vetterling, 1986.

[37] J. Mitroy and J.-Y. Zhang, *Physical Review A*, vol. 76, no. 3, p. 032706, 2007.

[38] J. Dhiflaoui, H. Berriche, M. Herbane, A. AlSehimi, and M. Heaven, *The Journal of Physical Chemistry A*, vol. 116, no. 43, pp. 10 589–10 596, 2012.

[39] P. Durand and J.-C. Barthelat, *Theoretica chimica acta*, vol. 38, no. 4, pp. 283–302, 1975.

[40] H. Berriche and F. X. Gadea, *Chemical physics*, vol. 191, no. 1-3, pp. 119–131, 1995.

[41] *The Journal of chemical physics*, vol. 97, no. 2, pp. 1144–1156, 1992.

[42] H. Berriche, *H. Ph.D. Thesis, Paul Sabatier University, Toulouse, France*, 1995.

[43] S. Duplaa, *Chem Phys. 1996, 105, 1492â1250*, 1996.

[44] S. Durand, Duplaa, *At. Mol. Clusters*, 1997.

[45] B. Ben El Hadj Rhouma, Ben Lakhdar, *Chem. Phys*, 2006.

[46] L. Blank, D. E. Weeks, and G. S. Kedziora, *The Journal of Chemical Physics*, vol. 136, no. 12, 2012.

[47] H.-J. Werner and P. J. Knowles, *The Journal of chemical physics*, vol. 89, no. 9, pp. 5803–5814, 1988.

[48] A. Berning, M. Schweizer, H.-J. Werner, P. J. Knwles, and P. Palmieri, *Molecular Physics*, vol. 98, no. 21, pp. 1823–1833, 2000.

[49] R. B. Bernstein, *Atom-molecule collision theory: a guide for the experimentalist*. Springer Science & Business Media, 2013.

[50] H. Margenau and N. R. Kestner. Elsevier, 2013, vol. 18.

[51] R. L. Roy, *in Molecular Spectroscopy 1, (Chem. Soc. Spec. Periodical) edited by R.F. Barrow, D.A. Long, and D.J. Millin (Chemical Society, London*, 1973.

[52] E. Goll, H.-J. Werner, H. Stoll, T. Leininger, P. Gori-Giorgi, and A. Savin, *Chemical physics*, vol. 329, no. 1-3, pp. 276–282, 2006.

[53] A. A. Medvedev, V. V. Meshkov, A. V. Stolyarov, and M. C. Heaven, *Physical Chemistry Chemical Physics*, vol. 20, no. 40, pp. 25 974–25 982, 2018.

[54] W. Baylis, *The Journal of Chemical Physics*, vol. 51, no. 6, pp. 2665–2679, 1969.

[55] M. Marinescu and A. Dalgarno, *Physical Review A*, vol. 52, no. 1, p. 311, 1995.

[56] U. Volz and H. Schmoranzer, *Physica Scripta*, vol. 1996, no. T65, p. 48, 1996.

[57] C. Cohen-Tannoudji, B. Diu, and F. Laloé. Paris: Hermann, 1996.

[58] Y. Ralchenko, *http://physics. nist. gov/asd.*, 2011.

[59] C. G. Carrington and A. Gallagher, *Physical Review A*, vol. 10, no. 5, p. 1464, 1974.

[60] N. Allard and J. Kielkopf, *Reviews of modern physics*, vol. 54, no. 4, p. 1103, (1982).

[61] A. Royer, *Physical Review A*, vol. 22, no. 4, p. 1625, (1980).

[62] P. Moroshkin, V. Lebedev, and A. Weis, *Physical Review AâAtomic, Molecular, and Optical Physics*, vol. 87, no. 2, p. 022513, (2013).